Reports on Progress in Physics

High-lying collective rotational states in nuclei

To cite this article: A Bracco and S Leoni 2002 *Rep. Prog. Phys.* **65** 299

View the article online for updates and enhancements.

Related content

- Rotation of warm nuclei and superdeformation
S Leoni and A Lopez-Martens
- Pairing correlations of nucleonsand multi-nucleon transfer between heavy nuclei
W von Oertzen and A Vitturi
- A historical overview of nuclear structure studies in Strasbourg Laboratories: instrumentation, measurements and theory modelling—hand-in-hand
F A Beck

Recent citations

- Projected shell model analysis of structural evolution and chaoticity in fast-rotating nuclei
Long-Jun Wang *et al*
- Single particle versus collectivity, shapes of exotic nuclei
Andrea Jungclaus

IOP ebooks™

Bringing together innovative digital publishing with leading authors from the global scientific community.

Start exploring the collection–download the first chapter of every title for free.

This content was downloaded from IP address 159.149.207.220 on 08/03/2021 at 07:21

INSTITUTE OF PHYSICS PUBLISHING REPORTS ON PROGRESS IN PHYSICS

Rep. Prog. Phys. **65** (2002) 299–352 PII: S0034-4885(02)07794-1

High-lying collective rotational states in nuclei

A Bracco and S Leoni

Dipartimento di Fisica, Universitá di Milano, and INFN sez. Milano, via Celoria 16, 20133 Milano, Italy

Received 24 September 2001, in final form 26 November 2001
Published 22 January 2002
Online at stacks.iop.org/RoPP/65/299

Abstract

A review of the latest works concerning the γ decay of high-lying collective rotational states is given. The study of warm rotating nuclei is based on several experiments made with large γ-spectroscopy arrays, including EUROBALL. The analysis techniques, mainly based on the fluctuations of counts of γ-coincidence spectra, are briefly described, while the obtained results are discussed in detail. The work presented here focuses on several properties of nuclei in the order to chaos transition region, such as (i) the importance of the two-body residual interaction in the description of the warm rotation; (ii) the collectivity of the excited rotational states; (iii) the conservation of quantum number with thermal energy; (iv) the dependence of the band mixing process on mass and deformation. Altogether, the results discussed in this review show a consistent picture of the problem of excited rotation in the regime of strongly interacting bands. The present limits and perspectives are also briefly given.

(Some figures in this article are in colour only in the electronic version)

 © 2002 IOP Publishing Ltd Printed in the UK

Contents

1. Introduction

The study of the nucleus at the limits of excitation energy and angular momentum is one of the central topics currently addressed with selective γ-spectroscopy measurements. In these extreme regimes nuclear structure studies are probing nuclear shapes and their evolution, the influence of thermal environments on low lying modes, collective rotation and giant resonances. In particular, the investigation of the simplest collective modes as a function of temperature and angular momentum has improved our knowledge of the properties of excited nuclei, shedding light on the transition from the cold ordered system to the chaotic regime of the compound nucleus.

In this context, the study of the rotational motion at finite temperature plays a crucial role in the understanding of the properties of the nuclear system beyond the mean field description, providing relevant information on the two-body residual interaction responsible for the band mixing process. The first experiments on rapidly rotating nuclei suggested that the E2 γ cascades would proceed down through rotational bands not only based on the ground states (yrast band), but also on excited configurations, up to the highest excitation energies. This would produce the continuous distributions observed in γ-coincidence spectra [1, 2], which could not be attributed to Compton scattering from the detectors [3]. Moreover, it was found that highly correlated γ-ray sequences of stretched E2 nature, characteristic of rotational bands, could only account for a small portion ($\leqslant$20%) of the unresolved spectrum intensity [4–6]. This suggested a spreading of the B(E2) strength of the excited rotational states over a wide energy interval [7], which could not be explained by pure cranking and γ-soft triaxial rotor calculations, posing a challenge to the theoretical understanding of the rotational motion in the excitation energy region where discrete spectroscopy is not possible.

At present, we know that, in medium mass nuclei, already at a few hundreds keV excitation energy above the yrast line, rotational bands are close enough in energy to be coupled by residual interactions. This implies that the 'simple' shell-model states that occur at low excitation energy will mix strongly over an energy range Γ_μ (called the *compound nucleus spreading width*) which corresponds to the average time spent by the compound nucleus in the intrinsic configuration. This leads to complicated stationary states that no longer correspond to any simple motion, as a part of the general order-to-chaos transition that the nucleus undertakes with increasing temperature. As a consequence, since the intrinsic states on which the rotational bands are built react differently to the Coriolis and centrifugal forces, the rotational degree of freedom becomes *damped* in the sense that the electric quadrupole decay from a single state at spin I will not go to a unique final state at $I-2$, but will exhibit a spectrum of final states, all at spin $I-2$. This mechanism is known as *damping of rotational motion* [8,9]. The probability for populating the final states is controlled by a strength function, whose width at half maximum is called the *rotational damping width* $\Gamma_{\rm rot}$. In the case of nuclear rotational damping it is important to note that, in contrast to the general definition of damping in which some simple degrees of freedom spread into more complicated degrees of freedom, all the admixed states are rotational: therefore the rotational motion itself is not damped. It is rather the rotational character of the levels that it is damped.

In the last two decades, considerable effort has been given to the study of the rotational motion at finite temperature, trying to address several questions related to the damping phenomenon. In particular, one would like to know (i) how large is the damping width $\Gamma_{\rm rot}$, and possibly also the compound damping width Γ_μ; (ii) what is the shape of the strength function associated with the stretched quadrupole decay in the damped region; (iii) at which energy rotational damping sets in, and how gradual the process is; (iv) whether or not the process depends on the intrinsic nuclear configuration, therefore leading to different effects in

connection with different quantum numbers of the shell-model states; (v) how high in excitation energy one has to go before a fully chaotic regime is reached. From the analogy between compound states of strongly rotating nuclei and the phenomenon of nuclear magnetic resonance (NMR), a schematic yet realistic model of rotational damping has been formulated [8, 9]. In the model, the average properties of the rotational damping width have been studied, focusing in particular on its dependence on the mass number A, the nuclear shape deformation ϵ, the angular momentum I and the intrinsic excitation energy U of the nucleus. Simple laws for the dependence of rotational damping on A, ϵ, I and U were predicted and lately confirmed with more realistic calculations [10].

Experimentally, the first works on the rotational quasi-continuum were mainly based on studies of the landscape of γ-coincidence spectra of $A \approx 160$ nuclei, in comparison with simulation calculations of the γ-decay cascades [11, 12]. This allowed the general features of the spectrum landscape to be reproduced, and the order of magnitude to be extracted for both the average spreading width and the critical excitation energy at which damping sets in. However, due to the strong dependence on the cascade parameters reproducing the average properties of the thermal rotation (e.g. moment of inertia, alignments, level density, damping width, etc), no precise estimates could be obtained, neither could a more quantitative analysis be performed. In addition, although rotational damping was the most plausible mechanism causing the observed quasi-continuum distribution in γ-coincidence spectra, no direct evidence was obtained which could rule out other possible explanations. In fact, large irregularity in the rotational spectrum could be related to a loss of collectivity with increasing temperature, which might be caused, for example, by shape fluctuations.

A considerable step forward in the understanding of thermal rotation was possible by a more quantitative study of γ–γ coincidence spectra, based on statistical analysis techniques [13]. In fact, the very existence of a *finite* number of γ-decay paths, below the particle binding energy, leads to enhanced fluctuations, whose magnitude is fixed by the number of paths. This differs from a purely statistical spectrum in which the events are randomly distributed directly over the experimental channels, and the relative fluctuations in the counting rate can be diminished at will simply by increasing the number of counts. Therefore, the analysis of the count fluctuations can be used to extract quantitative information from the quasi-continuum structures of γ-coincidence spectra, which are not accessible by discrete spectroscopy techniques. The foundation and mathematical formulation of the method, together with a first analysis of γ–γ coincidence data of rare-earth nuclei, are explained in detail in [14].

In the present paper we intend to review the latest results mainly obtained using the most recently developed technique, namely the analysis of the fluctuations in the number of counts of γ-coincidence rotational spectra. In particular, studies of nuclei in different regions of mass and deformation are discussed. For normally deformed (ND) nuclei we present results for ^{164,168}Yb and ^{114}Te, while for superdeformed (SD) nuclei the case of ^{143}Eu is discussed. In all cases, large statistics experimental data together with cranked-shell model calculations at finite temperature are available. This review is organized as follows. In section 2 the general experimental features of one-, two- and three-dimensional γ-coincidence spectra will be described, pointing at the signature and the properties of the damped rotation. In section 3 the recently developed microscopic shell model able to describe the individual nuclear levels and the E2 transitions at finite temperature [10] is briefly reviewed. The model predicts some novel features of rotational damping and allows the effect of the various components of the residual two-body force, and the gradual approach to the compound nucleus regime, to be studied in detail. These microscopic calculations are also at the basis of realistic simulation calculations of γ decay [15], which allow the most appropriate comparison between data and model prediction.

A short review of the fluctuation technique is given in section 4. This experimental method has been largely employed to determine the basic nuclear properties of the warm rotation, such as: (i) the lifetimes of the quasi-continuum rotational states (section 5); (ii) the role played by the residual interaction (section 6); (iii) the dependence of the damping process on the intrinsic nuclear configuration (section 7); (iv) the validity of the quantum numbers (especially the projection K of the angular momentum on the symmetry axis) increasing heat energy (section 8); (v) the dependence of the damping process on the atomic mass (section 9) and nuclear deformation (section 10).

Therefore, the present paper gives a review of the recent experimental and theoretical achievements in the study of the warm rotation, aiming at answering some of the questions originally formulated. From the discussion here presented it is clear that the extensive work made so far has indeed allowed us to make good progress in the understanding of the structure of warm nuclei. However, as discussed in section 11, there are still basic questions which are not fully answered, mainly related to the precise determination of the rotational and compound nucleus widths [16] and to a new predicted scenario, the regime of *ergodic* rotational bands, in which chaotic intrinsic states are combined with ordered rotational motion [17, 18].

2. Quasi-continuum spectra from fusion evaporation reaction

A common property of γ-ray spectra from heavy-ion fusion–evaporation reactions is the presence of intense distributions of a quasi-continuum nature, populated by the decay of highly excited high spin states, below the particle binding energy. In particular, quasi-continuum structures can be identified both in one-dimensional and multi-dimensional γ-coincidence spectra, allowing the study of the properties of the nuclear system in the transition energy region from discrete states to compound nuclei.

In this section we will briefly describe the main features of single (1D), double (2D) and triple (3D) γ-rays coincidence spectra from high-spin rotational nuclei, focusing on the properties which will be mostly analysed by the techniques discussed in the present review.

2.1. One-dimensional (1D) spectra

The simplest approach in the study of thermally excited rotational motion consists in the one-dimensional (1D) analysis of the data, which allows us to investigate several properties of the γ-ray intensity distribution. In particular, from 1D spectra one can deduce the average multiplicity of the γ cascades, the multipolarity of the transitions, the moment of inertia and the lifetimes. These observables can be employed to shed light on the rotational collectivity of the different spectral components, as described in this section in connection with data on the nucleus ^{164}Yb.

Figure 1 shows in logarithmic scale a 1D background subtracted spectrum, corrected for the detector efficiency, collecting the entire decay flow of ^{164}Yb, which is known to be a good rotor already at low spin and low internal energy [19]. The data were obtained with the EUROGAM II [20] array using the reaction ^{30}Si +^{138}Ba at the bombarding energies of 140, 145, 150, 155 MeV, corresponding to maximum angular momenta of 54, 59, 64, 68$\hbar$ [21, 22]. As observed in previous works on nuclei of the same mass region and deformation [23], three main components can be recognized in the spectrum: (i) the strong discrete peaks of the yrast band, extending up to $E_\gamma \approx 1$ MeV; (ii) the statistical E1 tail at energies $E_\gamma > 1.4$ MeV, which can be described over the entire energy region by the function $E_\gamma^3 \exp(-E_\gamma/T)$, with $T \approx 0.34$ MeV (broken curve in the figure); and (iii) a pronounced bump in the region $1 < E_\gamma < 1.4$ MeV, populated by damped transitions of stretched E2 character.

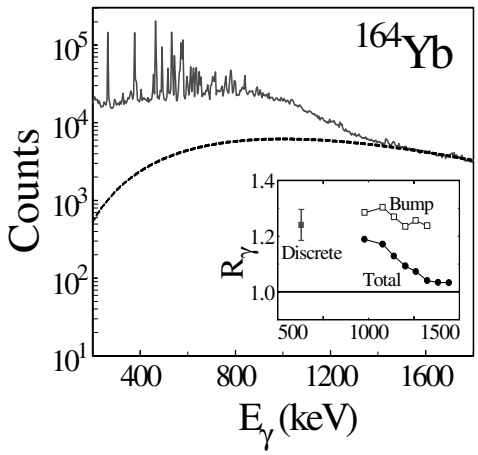

Figure 1. One-dimensional spectrum of ^{164}Yb, obtained by gating on low spin transitions of the ground state band which select the entire decay flow of the nucleus. The broken curve corresponds to an extrapolation of the E1 statistical tail by the function $E_\gamma^3 \exp(-E_\gamma/T)$, with $T \approx 0.34$ MeV. The inset of the figure shows the anisotropy R_γ of the total spectrum (full circles), of the continuum bump (open squares) and of purely stretched E2 low spin discrete transitions of ^{164}Yb (full squares) (adapted from [22]).

The multipolarity of the different spectral components observed in the 1D spectrum can be deduced from the angular anisotropy $R_\gamma(E_\gamma)$ defined as the ratio of the intensity of the spectrum at different angles (for example, forward and 90°). The inset of figure 1 shows the anisotropy $R_\gamma(E_\gamma)$ of the total spectrum (full circles) and of the bump (open circles), the latest being obtained after subtracting from the total spectrum the E1 contribution, assumed to be isotropic. As one can see, the anisotropy of the transitions of the bump is found to be close to the average value extracted from the analysis of purely stretched-E2 discrete transitions of ^{164}Yb (full square in the figure), confirming the rotational character of the continuum bump. Similar features have also been observed in 1D spectra gated on the $(\alpha, \pi) = (0, +)$, $(0, -)$ and $(1, -)$ intrinsic configurations of ^{164}Yb, as reported in [22]. In all three cases the analysis has shown the existence of a pronounced bump of rotational transitions in coincidence with the different low-lying (α, π) structures, giving a good basis for the investigation of the properties of the configuration dependence of the rotational motion at excitation energies where the damping phenomenon dominates strongly. This will be discussed in sections 7 and 8.

The rotational character of the continuous bump is also confirmed by the analysis of 1D spectra measured at different bombarding energies, as shown in figure 2 for the nucleus ^{164}Yb [24]. It is found that not only the intensity of the continuous distribution increases with bombarding energy/spin (panel (a)), but also the average γ-ray energy of the rotational bump moves towards higher values. This can be seen from the distributions shown in figure 2(b), obtained as a difference between spectra at two consecutive bombarding energies. This is the expected behaviour for rotational nuclei up to transition energies corresponding to the maximum value of the angular momentum that the nucleus can sustain, as observed in several cases, from well deformed nuclei of the rare earth region [23–25], to lighter deformed nuclei with mass $A \approx 110$ [24, 26], to superdeformed systems [27]. As discussed in section 9, the analysis of such difference spectra can be used to obtain an upper limit for the rotational damping width $\Gamma_{\rm rot}$.

Information on the dynamical moment of inertia $\Im^{(2)}_{\rm eff}$ of the quasi-continuum rotational transitions can be obtained from the height of the continuous bump. In fact, as described in [28, 29], if the damped transitions follow, on average, the main properties of the nuclear

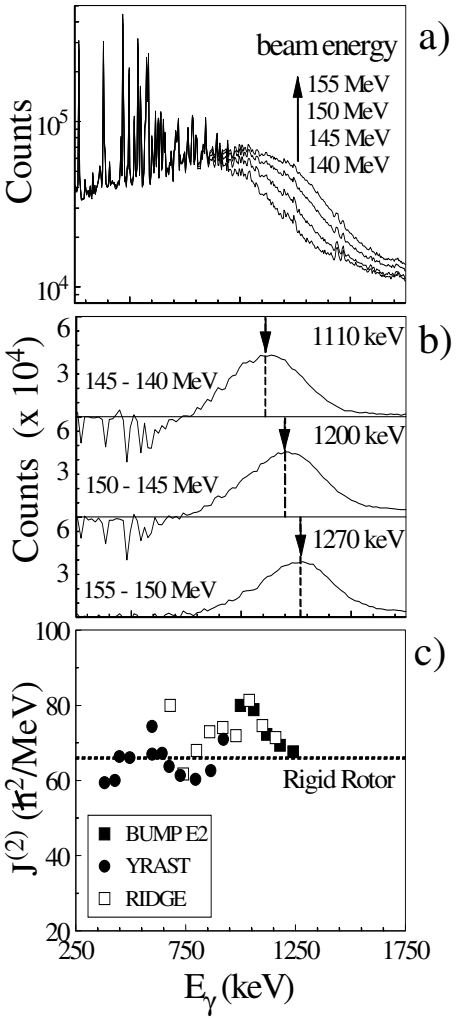

Figure 2. (*a*) γ spectra of ^{164}Yb measured at different bombarding energies. The arrow indicates that the spectrum with the lowest number of counts in the continuum distribution corresponds to the lowest bombarding energy. (*b*) Differences between two consecutive bombarding energies. The arrows indicate the positions of the centroids of the distributions. (*c*) The dynamical moment of inertia extracted from experimental analysis of the yrast transitions, ridges and E2 bump, as compared with the expected value for a rigid rotor (adapted from [24]).

rotation, their energies can be related to the average first and second moment of inertia $\Im^{(1)}_{\rm eff}$ and $\Im^{(2)}_{\rm eff}$ by the same relations satisfied by the discrete transitions, namely $\langle E_\gamma \rangle = 2\hbar^2/\Im^{(1)}_{\rm eff}$ and $\Delta E_\gamma = \langle E_{\gamma_1} - E_{\gamma_2} \rangle = 4\hbar^2/\Im^{(2)}_{\rm eff}$. This implies that, for a given number of E2 transitions, the bump will be more compressed if $\Im^{(2)}_{\rm eff}$ is large (being ΔE_γ small), and more stretched out if $\Im^{(2)}_{\rm eff}$ is small. Consequently, the height $H(E_\gamma)$ of the 1D quasi-continuum spectrum, after subtracting the E1 statistical component and normalizing the area to the absolute multiplicity of the rotational cascades, can be related to the effective moment of inertia $\Im^{(2)}_{\rm eff}$ by the relation

$$\frac{H(E_\gamma)}{f(E_\gamma)} = \frac{{\rm d}N}{{\rm d}E_\gamma} = \frac{\Im^{(2)}_{\rm eff}}{4\hbar^2}. \tag{1}$$

Here, ${\rm d}N/{\rm d}E_\gamma$ is the number of counts per unit interval, while $f(E_\gamma)$ is the feeding function, namely the fraction of observed population which goes through a given γ-ray interval. The quantity $f(E_\gamma)$ can be evaluated from spectra measured at different bombarding energies, as described in [28, 29]. Figure 2(*c*) shows the results for the effective moment of inertia $\Im^{(2)}_{\rm eff}$ of the bump for the nucleus ^{164}Yb (full squares) together with the average values for the yrast

transitions (full circles) and for the excited rotational bands (open squares) producing ridge structures in γ–γ spectra, as will be discussed in section 2.2 [24]. The quantity $\Im^{(2)}_{\rm eff}$ extracted from the quasi-continuum states is an effective moment of inertia, meaning that the E2 decay paths can proceed on average along an envelope of bands with different configurations. As one can see, the moments of inertia associated with near-yrast bands and with damped transitions show very similar values, slightly higher than for a rigid rotor, especially in the region above 1 MeV, confirming the collective character of the continuous distribution.

Besides all previous observations, the most convincing evidence for the collectivity of the bump in 1D spectra is given by the lifetime measurements of the γ decay populating the quasi-continuum distribution. As discussed in section 5, values of the fractional Doppler shifts for the edge of the rotational bump measured at forward and backward angles can be obtained using the analysis technique described in [23]. Due to the high γ-ray energies, it is most often found that the transitions at the edge of the bump are fully shifted, therefore providing only an upper limit $\approx 10^{-14}$ s for the lifetimes of the quasi-continuum states. This can be taken as further support for the strong collective character of the thermal rotation, although a definite value for the quadrupole deformation of the damped transitions can only be obtained from the analysis of the valley region of γ–γ coincidence spectra at lower transition energies [21], as discussed in section 5.

2.2. Two-dimensional (2D) spectra

A more direct evidence of the rotational pattern of unresolved transitions can be achieved by examining $E_{\gamma_1} \times E_{\gamma_2}$ coincidence spectra [14, 25]. Systematic studies in the rare earth region have revealed that the unresolved transitions of regular rotational bands form ridges parallel to the $E_{\gamma_1} = E_{\gamma_2}$ diagonal, while damped transitions from the mixed rotational bands fill the valley region. This allows for a clear separation of the contributions from the two different rotational regimes. The two-dimensional (2D) rotational pattern can be clearly seen in figure 3(*a*), showing a section of a γ–γ coincidence matrix of ^{168}Yb [14]. In the spectrum the Compton and the other uncorrelated events have been reduced by the standard COR treatment with a reduction factor of ≈ 0.7 [4, 14]. In the same figure, panel (*b*) and (*c*) show perpendicular cuts across the $E_{\gamma_1} = E_{\gamma_2}$ diagonal, at the average transition energies $\langle E_\gamma \rangle = (E_{\gamma_1} + E_{\gamma_2})/2 = 820$ and 1000 keV, respectively. The width of the cut is chosen to be $\Delta E_\gamma = 4\hbar^2/\Im^{(2)} \approx 60$ keV, corresponding to the average spacing between rotational transitions. In both cases a regular ridge–valley structure is observed, even after removal of the known intense discrete transitions from the right-hand side of the spectrum ($E_{\gamma_2} > E_{\gamma_1}$). As shown by the arrows in the figure, the energy separation between the two inner ridges, equal to $2 \times \Delta E_\gamma = 2 \times 4\hbar^2/\Im^{(2)}$, can be used to obtain the dynamical moment of inertia of the discrete excited rotational bands, as given in figure 2(*c*) for the nucleus ^{164}Yb.

2.3. Three-dimensional (3D) spectra

The coincidences carrying rotational energy correlations form ridge–valley structures not only in 2D spectra but also, even more pronounced, in 3D coincidence matrices. This is clearly illustrated in figure 4, where double and triple γ coincidence data from a EUROGAM I [30] experiment on ^{168}Yb nuclei are shown. The ^{168}Yb nuclei were produced in excited states of high angular momentum by the reaction ^{124}Sn(^{48}Ca, xn)$^{172-x}$Yb, at a beam energy of 210 MeV and with a ^{124}Sn target consisting of two unbacked stacked foils each of thickness 0.5 mg/cm^2. Approximately 8×10^8 coincidence events Compton suppressed with fold $\geqslant 3$ were collected [31, 32].

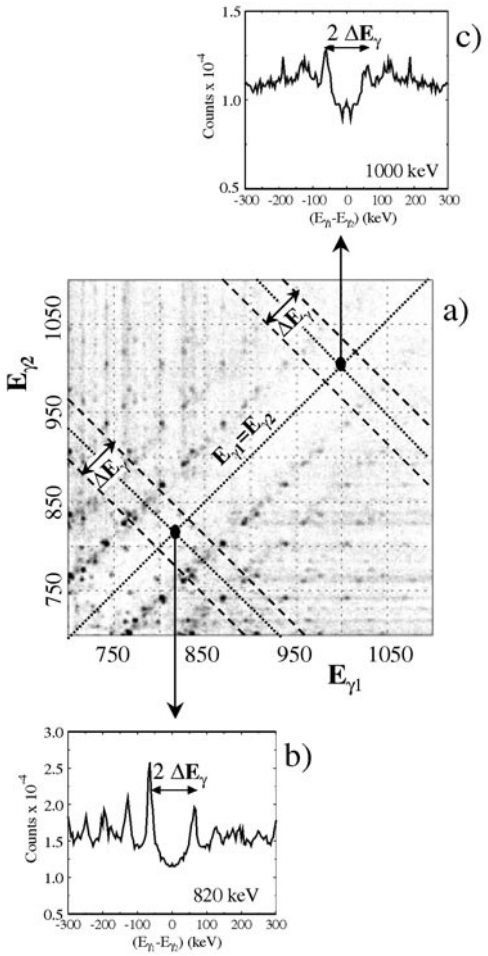

Figure 3. The rotational pattern of the excited rotating nucleus ^{168}Yb, as observed in the γ–γ coincidence spectrum: (*a*) section of the 2D matrix covering the (700, 1100) keV × (700, 1100) keV γ-ray interval. The regions of the spectrum corresponding to the projections shown in panel (*b*) and (*c*), centred at the average transition energies $\langle E_\gamma \rangle = 820$ and 1000 keV with a width $\Delta E_\gamma = 4\hbar^2/\Im^{(2)}$, are delimited by broken lines. In the 1D projections the contributions from known discrete transitions have been subtracted from the right-hand side of the spectrum ($E_{\gamma_1} > E_{\gamma_2}$), resulting in a weaker ridge structure. The separation between the ridges and its relation with ΔE_γ, corresponding to the average spacing between consecutive transitions in a regular rotational band, is indicated by arrows in panels (*b*) and (*c*).

In this case the data have been sorted into a 2D high-resolution matrix with 0.5 keV/ch, selecting in the best possible way the final ^{168}Yb nucleus, and into a 3D low resolution cube with 4 keV/ch. Both 2D and 3D spectra have been background subtracted by the COR method, which needs a background reduction factor, chosen in this case to be 0.4 and 0.5, respectively [4, 14].

By cutting out slices of the 3D cube, centred at the *tilted rotational planes*, the ridges are picked out and much enhanced above the surrounding background, as compared with the corresponding ridge structure in the γ–γ matrix. Each rotational plane, defined by the equation

$$E_{\gamma_1} - E_{\gamma_3} = N(E_{\gamma_3} - E_{\gamma_2}) \pm \delta/2 \tag{2}$$

with $N = 1, 2, 3, \ldots$ [32], selects in fact different types of coincidences along rotational bands, as schematically shown on the left-hand side of figure 4. The $N = 1$ plane will contain, for example, three consecutive γ-ray transitions, or γ-ray number 1, 3 and 5 out of five consecutive, etc. The $N = 2$ plane will contain γ-ray number 1, 3 and 4 out of four consecutive transitions, and so on. The right-hand part of figure 4 shows typical perpendicular cuts with a width $\Delta E_\gamma = 4\hbar^2/\Im^{(2)} \approx 60$ keV at $\langle E_\gamma \rangle = 900$ keV, on the final 2D spectrum (*a*) and on the symmetrized tilted rotational planes (only $N = 1$ is, in fact, born symmetric), defined by equation (2) with $N = 1, 2$ and 3 (part (*b*)–(*d*)). As one can see, the ridge structures in the

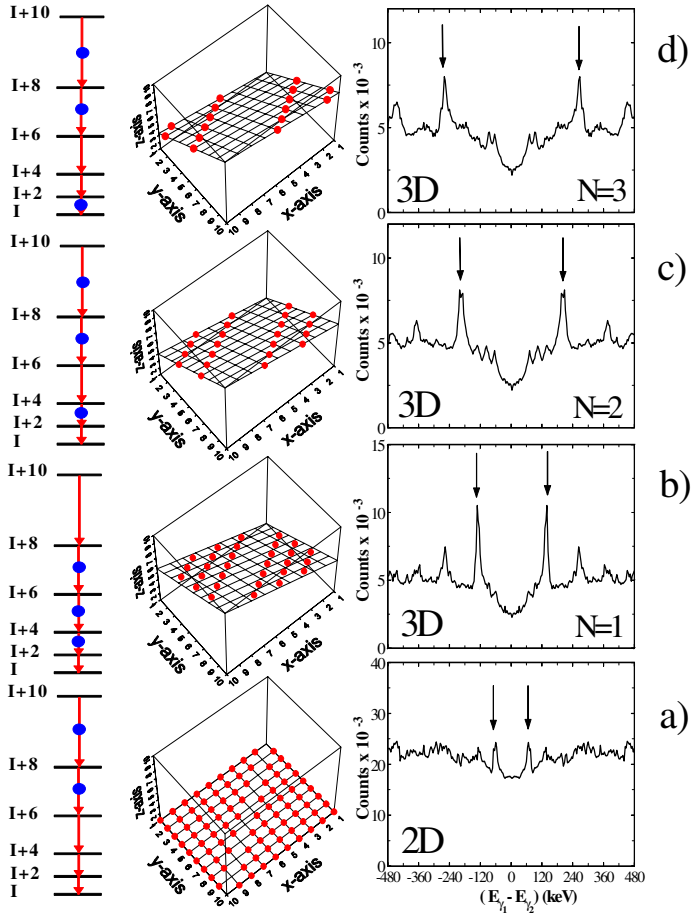

Figure 4. The left-hand side of the figure shows a schematic illustration of the rotational correlation pattern forming ridges in both 2D (*a*) and 3D tilted rotational planes, defined by equation (2), with $N = 1, 2$ and 3 ((*b*), (*c*) and (*d*)). The coincidence combinations selected by the different planes are indicated by circles in the rotational cascades. The right-hand side of the figure shows corresponding perpendicular cuts, 60 keV wide, at the average transition energy $\langle E_\gamma \rangle = 900$ keV, on the 2D matrix and on the tilted rotational planes of ^{168}Yb. The arrows points at the innermost ridge structure observed in the different spectra (adapted from [32]).

3D planes are significantly stronger than in the 2D spectrum, as expected, standing out on the background of damped, statistical and Compton scattered transitions.

As discussed in section 6, the analysis of the ridge structures in 2D and 3D spectra, namely as a function of the length of the rotational cascades, can be used to obtain information on the strength of the residual interaction, responsible for the onset of rotational damping at high excitation energy above the yrast line.

3. The theoretical approach: realistic band mixing calculations

Since the discovery of quasi-continuum rotational structure in γ-coincidence spectra [5], considerable work has been done to explain the experimental findings. Leander was the first to suggest a spreading of the E2 decay over many states, as a consequence of the mixing between

close lying rotational bands [7], while a schematic model describing the average properties of the rotational damping width can be found in [8,9]. Lately, more consistent calculations have been performed with the cranking model, as reported in [10,33]. In the present section we will mainly focus on the microscopic cranked shell model calculations of [10], which have been extensively used in comparison with the experimental data from different regions of mass and deformation discussed here. The model is able to describe the individual nuclear levels and E2 transitions in the warm region, aiming at studying in detail the transition from the discrete rotational bands into the region of rotational damping. As discussed in section 3.2, the microscopic calculations are also at the basis of realistic simulation calculations of the γ-decay cascades. This has allowed us for the first time to produce calculated spectra with meaningful fluctuations, which can be analysed by statistical analysis techniques as the experimental data.

3.1. The band mixing model

Microscopic cranked shell model calculations have been performed to investigate the rotational motion at finite temperature and extract more detailed information on the transition from regular to damped regime [10]. The model, originally developed for the rare earth nucleus ^{168}Yb, has been successfully used to study different regions of mass and deformation [10, 16]. In the case of ^{168}Yb, at each even spin value between $I = 20\hbar$ and $60\hbar$, the lowest 1000 rotational bands above yrast have been obtained by cranked shell model calculations, without including pairing. In the model the single-particle basis is obtained by cranking the particle–hole states of a Nilsson potential (with fixed deformation parameters $\beta = 0.25$ and $\gamma = 0^\circ$), representing the intrinsic excitations of the rotational nucleus. Each np-nh configuration forms a rotational band. The rotational bands are then mixed by a two-body residual interaction of surface delta type (SDI) with standard interaction strength $V_0 = 27.5$ MeV/A [34]. In this way, the lowest 500 mixed bands covering, in the case of ^{168}Yb, the excitation energy interval up to about 2.3 MeV above the yrast line have been generated. In addition, the transition probabilities S_{ij} between all states i, j at spin I, $(I - 2)$ have been calculated from the overlap of the wavefunctions at the two spins.

As schematically shown in figure 5, the microscopically calculated E2 strength distributions as a function of the excitation energy above yrast are characterized by a progressive fragmentation of the rotational strength. This can be clearly seen in the (a), (b) and (c) insets, where the distribution of rotational transition strength is given at the excitation energy above yrast $U = 0$, 657 and 1640 keV, averaging over bins of 5 levels. In the right part of the figure we show the branching number

$$n_{\text{branch}} = \left(\sum_j S_{ij}^2 \right)^{-1} \tag{3}$$

which gives the effective number of E2 branches out of a single state. If we define regular rotational bands as the bands with $n_{\text{branch}} < 2$, we see from figure 5 that a gradual transition from undamped to damped motion occurs between 800 and 1200 keV, so that we can say that in the nucleus ^{168}Yb the onset of rotational damping takes place around $U_0 \approx 1$ MeV. This value is in agreement with the experimental analysis of γ–γ coincidence data, as discussed in section 6. It is worth noticing that the definition of U_0 is, to some extent, arbitrary, because the transition from the regime of pure rotational bands to the regime of full rotational damping, in which it is possible to define a B(E2) strength function, takes place more gradually than it is here proposed. In fact, as it turns out from a closer look at the microscopic calculations, scars of discrete rotational bands extending over few spin values are found to exist even at excitation energies where the damping phenomenon dominates strongly [35].

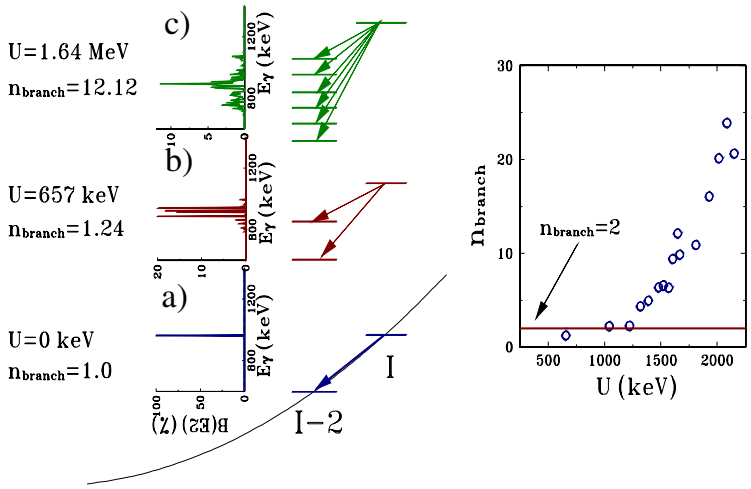

Figure 5. On the left-hand side of the figure we illustrate schematically the gradual fragmentation of the E2 rotational strength, as obtained by the band-mixing calculations described in section 2. The E2 strength distribution from initial levels placed at excitation energy $U = 0$, 657 and 1640 keV are given in the insets (*a*), (*b*) and (*c*). The right part of the figure displays the branching number n_{branch}, defined by equation (3), as a function of the excitation energy above the yrast line. The full line, corresponding to $n_{\text{branch}} = 2$, defines the onset energy for rotational damping.

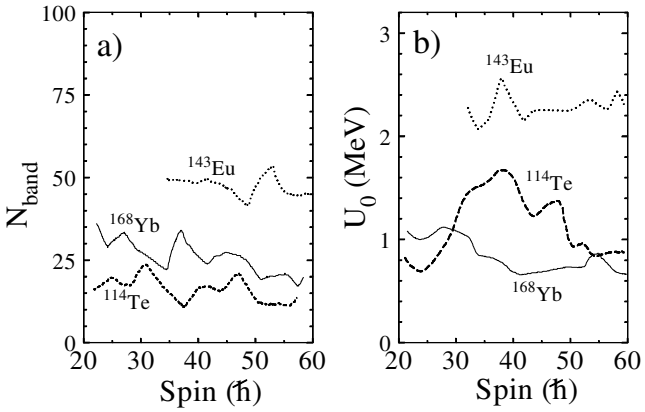

Figure 6. The number N_{band} of discrete rotational bands (*a*) and the onset energy U_0 of rotational damping for ND ^{114}Te and ^{168}Yb nuclei and for the SD nucleus ^{143}Eu (*b*), as a function of spin (adapted from [16]).

As reported in [16], the microscopic calculations predict large variation of rotational damping as a function of deformation, mass number and nuclear species. This is shown in figure 6, for the normal deformed (ND) nuclei ^{114}Te and ^{168}Yb and for the superdeformed (SD) nucleus ^{143}Eu, to which we mainly refer in connection with the experimental data presented here. As one can see, the number of discrete rotational bands which lie near the yrast line, surviving against rotational damping, varies considerably from nucleus to nucleus (panel (*a*)). This is also true for the onset energy U_0 of rotational damping (panel (*b*)), mainly reflecting the differences in level density between the various nuclear systems.

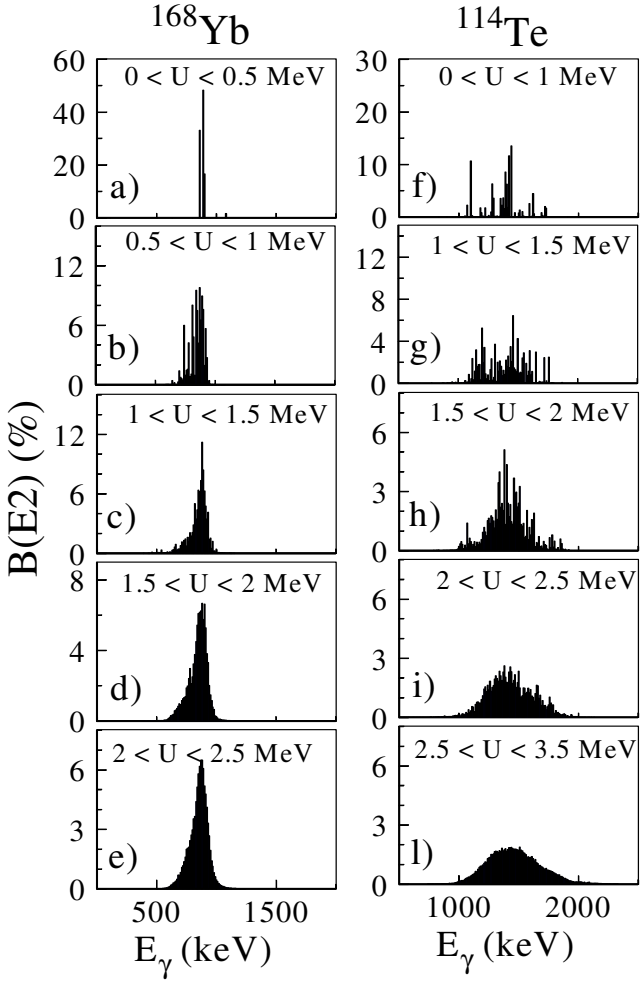

Figure 7. The B(E2) strength distributions for ^{168}Yb and ^{114}Te, corresponding to spin $30\hbar$, are shown in the left and right panels, respectively. They were obtained by band mixing calculations [10] averaging over the intrinsic excitation energy intervals indicated in each panel.

As already pointed out in connection with figure 5, the main feature of the microscopic model relevant for the study of the continuum is the variation of the E2 rotational strength distribution with spin I and internal energy U. In figure 7 a number of B(E2) strength distributions for ^{168}Yb and ^{114}Te at spin $30\hbar$ are shown. There one sees that the mean value of the distributions does not depend on the internal energy U, as expected for typical γ transitions among levels of rotational bands satisfying the relation $E_\gamma = 2\hbar^2 I/\Im^{(1)}$. In contrast, the shape and the width of the B(E2) distribution are strongly affected by the intrinsic energy of the system. In particular, at high internal energy the distribution becomes rather smooth and wide as a consequence of the strong mixing of close lying states due to the residual interaction. In addition, large differences are observed between the two nuclei, especially for the width of the B(E2) distribution, namely the rotational damping width $\Gamma_{\rm rot}$. This is also illustrated in figure 8, where the rotational damping width is given for ^{168}Yb, ^{114}Te and ^{143}Eu nuclei, as a function of spin.

As described in the original rotational damping model by Lauritzen *et al* [8], the width of the B(E2) strength is directly related to the spreading of the rotational frequency $\Delta\omega$ of the

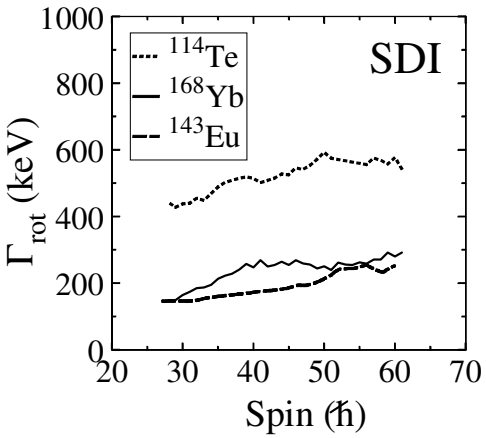

Figure 8. The rotational damping width Γ_{rot} extracted from standard deviation of the microscopically calculated B(E2) rotational strength [10, 80], for the ND ^{168}Yb and ^{114}Te nuclei and for the SD nucleus ^{143}Eu, as a function of spin.

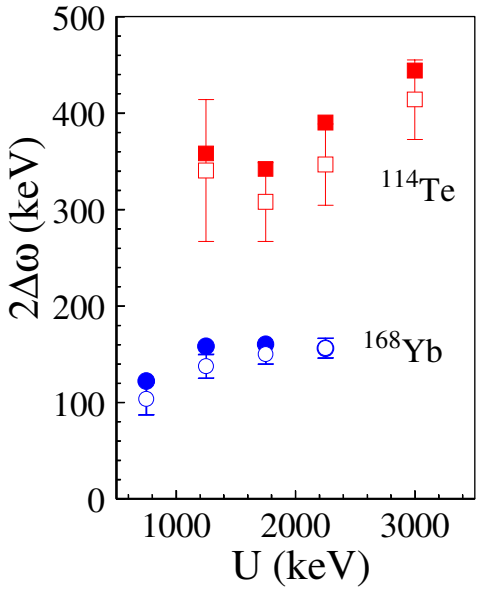

Figure 9. Twice the values of the dispersion $\Delta\omega$ in rotational frequency are shown by open symbols with error bars for the cranked shell model bands of ^{168}Yb and ^{114}Te nuclei at spin $30\hbar$. The values are given as a function of the internal energy U, averaging over the same excitation energy interval shown in figure 7. The full symbols represent the Γ_{rot} values obtained from the width of the corresponding B(E2) strength shown in figure 7.

different unperturbed rotational bands, being $\Gamma_{rot} = 2\Delta\omega$. In figure 9 values of $2\Delta\omega$ deduced from the transition energies of the cranked shell model bands of ^{168}Yb and ^{114}Te at spin $30\hbar$ are plotted by points with error bars as a function of the internal energy U, averaging over the same excitation energy interval shown in figure 7, while the full symbols represent the Γ_{rot} values obtained from the width of the corresponding B(E2) strength shown in figure 7. Again one can notice the very different values of Γ_{rot} obtained for the two nuclei, and the consistency of Γ_{rot} with $2\Delta\omega$, in agreement with the prediction of the schematic model of [8] (see also the discussion in section 9).

Since rotational damping is mainly controlled by the configuration mixing caused by the residual interaction, the dependence on the two-body force has been tested in the model in the specific case of ^{168}Yb [10]. As discussed in section 6 in connection with the fluctuation analysis of the experimental data, substantial difference is found in the number of discrete regular bands (before damping sets in), depending on the type and the strength of the residual interaction. In particular, satisfactory agreement between data and model predictions is obtained when an SDI

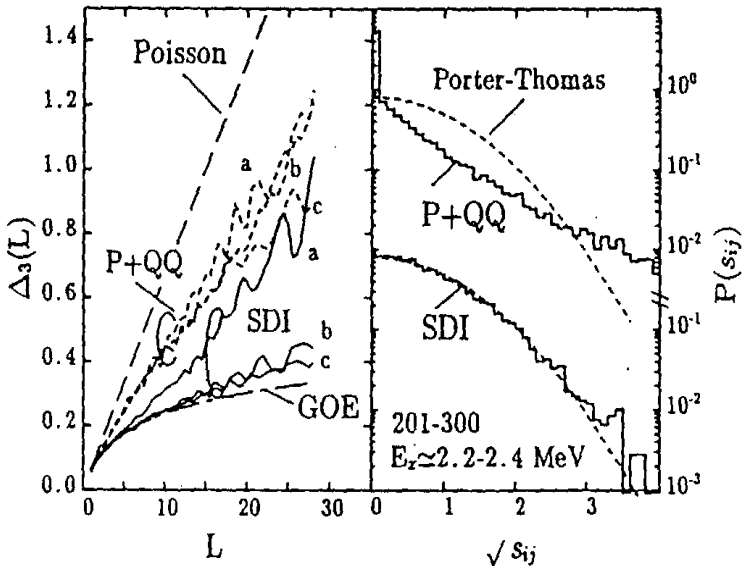

Figure 10. The left part of the figure shows the rigidity Δ_3 of the energy levels obtained from microscopic cranked shell model calculations including a two-body residual interaction of SDI type (full lines) or of P + QQ type (short broken). The labels a, b and c refer to bins of 100 levels whose excitation energies above yrast are approximately 0.0–1.9, 1.9–2.2 and 2.2–2.4 MeV, respectively, for SDI, and 0.0–1.6, 1.6–1.9 and 1.9–2.1 MeV for P + QQ. The limit expected for the Δ_3 parameter in the case of Poisson and GOE distributions are also given. In the right-hand side of the figure the normalized strength distributions are calculated for the transitions from the 201–300th levels (corresponding to the third bin c), with γ-ray energies satisfying $0.9 < E_\gamma < 1.05$ MeV. The broken curves represent the Porter-Thomas distribution (from [36]).

residual interaction with standard strength and including all multiple components is employed, showing that rotational damping essentially originates from the high multiple terms.

The dependence of the statistical properties of the microscopically calculated levels on the type of interaction strength has also been investigated in terms of the rigidity parameter Δ_3 and of the normalized rotational strength $s_{ij} = S_{ij}/\langle S_{ij}\rangle$ [36, 37]. As shown in figure 10, as the intrinsic excitation energy U increases, the Δ_3 level statistics (left panel) and the normalized rotational strength (right panel) show a gradual transition from order to chaos, closely resembling, already at $U \geqslant 2$ MeV, the Wigner and Porter-Thomas distributions typical of the Gaussian orthogonal ensemble of random matrices. In contrast, a strong deviation from these limits is found in the case of the model employing a pairing plus quadrupole (P + QQ) residual interaction, confirming that the high-multiple terms contained in the SDI interaction are responsible for the mixing of the unperturbed rotational bands.

One can then conclude that, as discussed in [36, 37], the study of the rotational motion at finite temperature is an essential tool not only for shedding light on the properties of the nuclear many-body system beyond the mean field description, but also for understanding the mechanisms which bring the nucleus from an ordered regime to quantum chaos.

3.2. Microscopic simulation of the γ decay

In the last decade, considerable progress has been made in the experimental study of the thermally excited rotational motion by the use of a statistical analysis of the fluctuations of counts in γ–γ coincidence spectra [14]. The method, briefly reviewed in section 4, can be

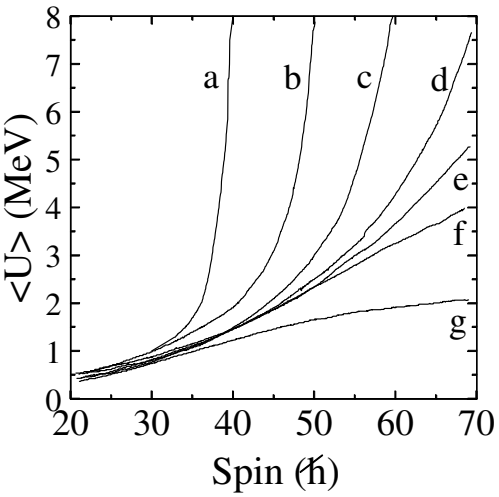

Figure 11. The average heat energy of the decay flow is calculated according to the model of [38], for various initial conditions, labelled by letters (a)–(g). The initial distributions are taken as Gaussian with standard deviation $\sigma = 1$ MeV. The initial angular momenta and heat energy are $(I_0, \langle U_0 \rangle) = (40, 8)$ (a), (50, 8) (b), (60, 8) (c), (70, 8) (d), (70, 5.5) (e), (70, 4) (f) and (70, 2) (g) (adapted from [38]).

used to determine the number of paths available to the nucleus in the course of the γ decay, therefore providing a quantity which is very sensitive to the different regions of excitation energy and spin. However, to make use of the power of the fluctuation analysis one needs to obtain similar information also from the theory. For the ridge structures observed in γ–γ coincidence matrices and populated by discrete excited rotational bands, the number $N_{\rm path}$ of decay paths can be estimated from the band mixing calculations described in section 3.1 by simply counting the number of two consecutive transitions having a B(E2) strength which does not branch to more than two levels, namely with $n_{\rm branch} < 2$, as discussed in connection with equation (3). In the case of the valley the situation is more complicated and the quantity $N_{\rm path}$ cannot be directly obtained from the calculations, since it strongly depends on the decay flow of the excited rotating nucleus. In fact, as shown in figure 11 [38], depending on the initial distribution of spin and excitation energy the γ decay of the rotating nucleus spans through very different regions of level densities, at least in the first quarter of the cascades, when the damping of the rotational motion dominates strongly. For this reason, to investigate in detail the region of rotational damping one needs not only to simulate the γ decay of the excited rotating nucleus from the residual entry distribution down to the yrast line, but also to construct simulated spectra of the same type of experimental data. In addition, in order to be able to apply to simulated spectra the same statistical analysis performed on real data, one needs to base the simulation of γ spectra on a finite number of levels, as the ones calculated, for example, by the band mixing model described in the previous section. This has been done in the simulation code MONTESTELLA [15], which is an extension of an earlier statistical code based on parametrizations of the physical quantities governing the thermal rotation (e.g. moment of inertia, alignments, level density, damping width, etc) [11].

In this connection, it is interesting to discuss the main features of the physical quantities entering into the simulation, namely the kinematic $\Im^{(1)}$ and dynamic $\Im^{(2)}$ moment of inertia of the rotational bands, the B(E1) and B(E2) strengths and the level density. The average values of the kinematic and dynamic moment of inertia for ^{168}Yb and ^{114}Te nuclei are shown in figure 12 for the microscopically calculated discrete rotational bands having $n_{\rm branch} < 2$, in comparison with the experimental values. While in the case of ^{168}Yb both the calculated kinematic and dynamic moment of inertia are rather similar to the experimental values, the same is not true in the case of the dynamic moment of inertia of ^{114}Te, the latter being smaller

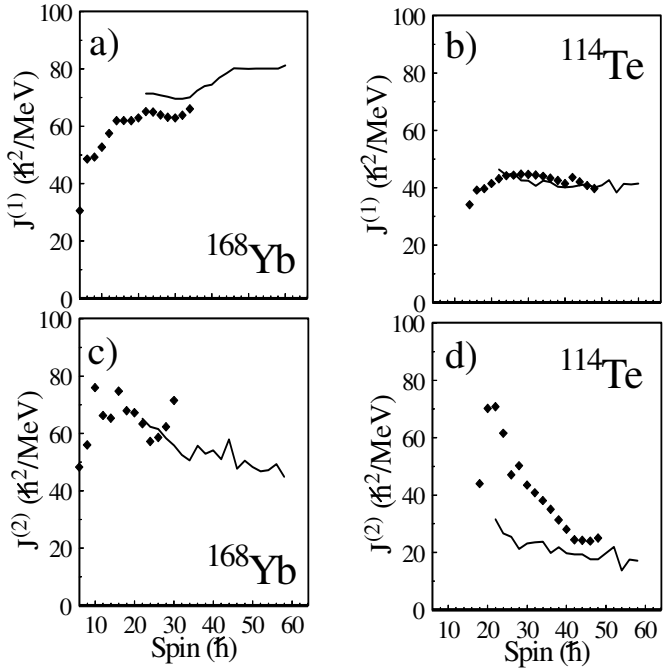

Figure 12. The average kinematic moment of inertia $\Im^{(1)}$ of the regular discrete bands having $n_{\text{branch}} \leqslant 2$, as obtained from band mixing calculation [10], are shown by full curves in comparison with the experimental values (diamonds), for ^{168}Yb and ^{114}Te nuclei ((*a*) and (*b*), respectively). A comparison of the same type is shown in (*c*) and (*d*) for the average dynamic moment of inertia $\Im^{(2)}$.

than in the experiment in the spin region 20–40$\hbar$. However, this disagreement turns out not to be a major drawback, since the value of the dynamical moment of inertia $\Im^{(2)}$ affects only the position of the ridges, as observed in connection with figure 3, and it does not influence the results concerning the central valley, which is well separated by the ridge structures. Also the value of n_{branch}, used to calculate the number of discrete rotational bands, is mainly controlled by the strength of the residual interaction and by the level density and it is not affected by the value of $\Im^{(2)}$.

Figure 13 shows the level density $\rho(U)$ of the microscopically calculated nuclear states of ^{168}Yb and ^{114}Te (open circles) and the extrapolated values obtained by fitting the microscopic levels with the Fermi gas level density function with fixed signature and parity

$$\rho(U) = \frac{\sqrt{\pi}}{48} \frac{\exp 2\sqrt{aU}}{a^{1/4}U^{5/4}} \tag{4}$$

which is appropriate for the cranked mean field description [39]. The corresponding value of the a parameter is also given in the figure. It is worth noticing that, experimentally, precise measurements of level density for rare earth nuclei in the excitation energy region below the particle binding energy exist only at low spins, as reported in [40–42]. In these works structures are observed in the level density curves at 1–5 MeV excitation energy, which have been attributed to a quenching of pairing correlations already at moderate temperature. This gives strong support to the use of the microscopic band mixing calculations of [10] in the description of the high-spin rotational motion at finite temperature, although pairing correlations are not explicitly included in the model.

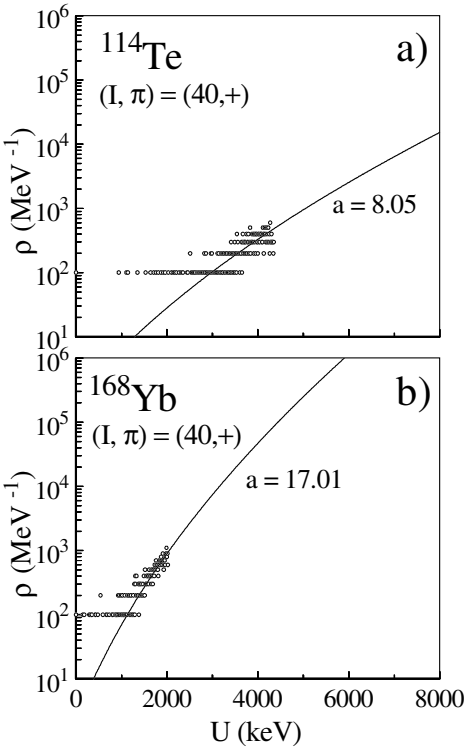

Figure 13. The level density of the calculated band mixing states with spin and parity $(I, \pi) = (40, +)$ for ^{114}Te (panel (a)) and ^{168}Yb (panel (b)). The full curves represent the extrapolated values obtained by fitting the microscopic levels with the Fermi gas level density function defined by equation (4). The level density parameter a fitting the calculated levels is also indicated.

In the MONTESTELLA simulation code the expression of the level density is used to calculate the E1 transition probability defined as

$$T(\mathrm{E1}, U_i) = H_{\mathrm{E1}} \int_0^{U_i} (U_i - U)^3 f_{\mathrm{GDR}}(U_i - U) \frac{\rho(U)}{\rho(U_i)} \, \mathrm{d}U. \tag{5}$$

Here the strength function f_{GDR} is given by the giant dipole resonance (GDR) of Lorentzian shape, which in the case of ^{168}Yb has a centroid $E_0 = 15$ MeV and a width $\Gamma_{\mathrm{E1}} = 5$ MeV. It is generally found that, in order to reproduce the average experimental intensity of low-lying bands, one has to reduce substantially the value of the tail of f_{GDR} by the hindrance factor H_{E1}, as compared to the value deduced assuming that the GDR exhausts the E1 sum rule [15, 26]. This is in agreement with previous theoretical studies [43]. In the region of discrete levels, the integral in expression (5) is replaced by a summation.

Figure 14 gives a schematic illustration of the γ decay in the spin-excitation energy plane, as it is simulated by the MONTESTELLA code via the E1–E2 competition from the residual nucleus entry distribution down to the yrast line. As shown in the figure, the simulated decay makes use of the level density ρ and the B(E2) strength function obtained from the microscopic band mixing calculations up to ≈2–3 MeV excitation energies above yrast, depending on the mass number. At higher excitation energies, up to the neutron binding energy, both quantities are extrapolated from the previously microscopically calculated values. In addition, as discussed earlier, the E1 strength is taken as the tail of the GDR and parametrized according to equation (5).

In figure 15(a) we show, as an example, a perpendicular cut on a γ–γ experimental spectrum of ^{168}Yb at the average transition energy $(E_{\gamma_1} + E_{\gamma_2})/2 = 920$ keV. The spectrum is compared with corresponding projections of simulated 2D matrices based on cranked shell

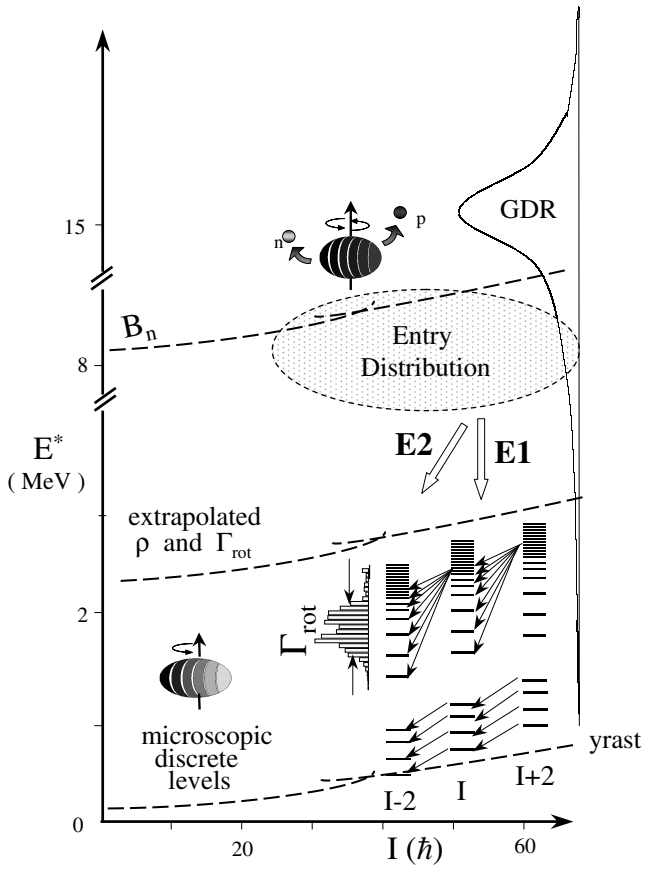

Figure 14. Schematic illustration of the γ-decay flow, as simulated by the MONTESTELLA code via E1–E2 competition from the residual nucleus entry distribution down to the yrast line [15]. The simulated decay makes use of the microscopically calculated levels and transition probabilities, extending up to ≈2.3 MeV above yrast in ^{168}Yb, while at higher excitation energy both level density and B(E2) strength are extrapolated from the microscopic levels. The E1 decay probability is calculated from the tail of the GDR according to equation (5).

model calculations including (*b*) or not (*c*) the SDI two-body residual interaction [15]. As one can see, the simulation based on mixed rotational bands is rather successful in reproducing the overall shape of the ridge–valley structure of the experimental distribution, giving strong support to the theoretical band mixing model.

One can then conclude that simulated spectra based on microscopic band mixing calculations, of similar kinds to those discussed in section 3.1, can be useful to sharpen the comparison between experiment and theory. This can be done both in terms of the gross features of the spectrum landscape, as shown in figure 15, but also by means of more sensitive quantities, like the number of decay paths, which can be extracted by a fluctuation analysis of the ridge and valley structures of γ–γ coincidence spectra, as discussed in the next section.

4. Experimental methods: statistical analysis of rotational spectra

In the last decade, a considerable step forward in the study of the warm rotation has been possible by the use of statistical analysis of γ-coincidence spectra. In fact, having to deal with

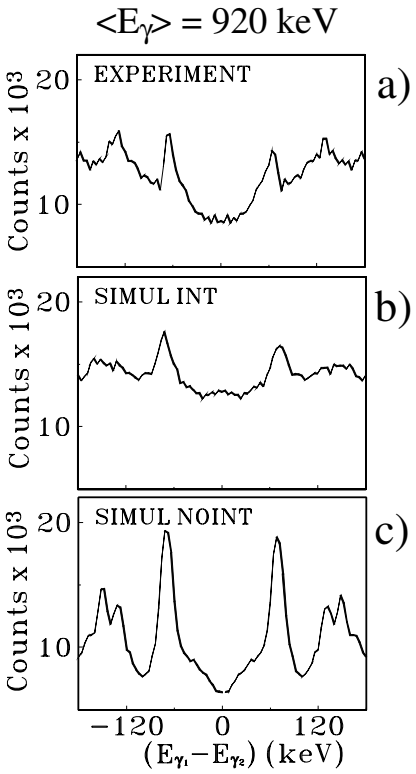

Figure 15. Perpendicular cuts, 60 keV wide, at the average transition energy $\langle E_\gamma \rangle = 920$ keV, on experimental (*a*) and simulated (*b*) and (*c*) γ–γ coincidence matrices of ^{168}Yb. The simulated spectra have been based on cranking calculations including (*b*) or not (*c*) a two-body residual interaction of surface delta type [10, 15]. The most intense discrete transitions were subtracted from the right-hand side of the spectra in all cases (adapted from [15]).

spectra mainly constituted by continuous distributions, it becomes difficult to extract detailed nuclear-structure information, particularly about the picture of rotational damping. Therefore, a statistical treatment of the counting rates has been developed. The method has turned out to be instrumental in obtaining quantitative information on the damping process, together with the first clear experimental evidence of the phenomenon. Fluctuations in rotational spectra and their interpretation were first discussed by Stephens in [44], although statistical methods have been previously applied to nuclear physics [45]. In this section, we briefly recall the basic features of the statistical analysis technique, while the foundation and the mathematical formulation of the method are discussed in detail in [14, 22].

The study of the fluctuations of counts of double (or higher fold) coincidence spectra is based on the fact that the γ decay that cools the compound system along damped rotational bands makes use of all possible *decay paths*, namely a sequence of 2 (or more) transitions in coincidence, fewer times than when the process moves along sharp, discrete bands close to the yrast band. Therefore, since the larger the number of choices available for each event is, the smaller are the associated fluctuations in the counting rate and *vice versa*, one is able to analyse rotational γ-decay spectra from compound nuclei in terms of fluctuations and recognize the regime where the decay branches out to many final states, as opposed to the discrete rotational regime where the decay goes to a single final state along a rotational band. In fact, while a purely statistical spectrum displays fluctuations simply due to the counting statistics, the very existence of a *finite number* $N_{\rm path}^{(2)}$ of decay paths in the rotational decay will lead, in a γ–γ coincidence spectrum, to enhanced fluctuations, whose magnitude turns out to be fixed by the number of paths through the simple expression

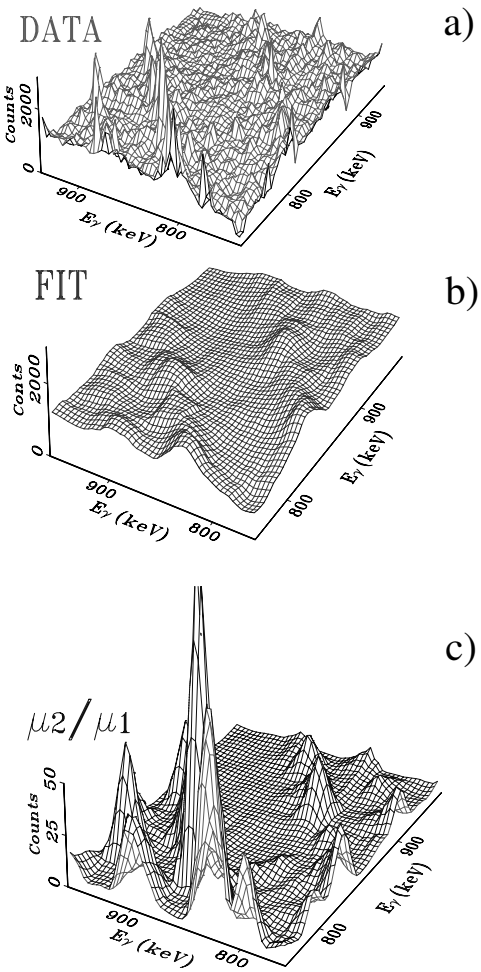

Figure 16. 2D coincidence spectra associated with the decay of ^{168}Yb for the experimental data (*a*) (background subtracted with the COR treatment), and for the corresponding smooth polynomial fit (*b*) and μ_2/μ_1 fluctuation spectrum (*c*). The known discrete lines have been removed from the right-hand side of the COR spectrum before the fluctuation analysis is performed (adapted from [14]).

$$N_{\text{path}}^{(2)} = \frac{N_{\text{eve}}}{\frac{\mu_2}{\mu_1} - 1} \times \frac{P^{(2)}}{P^{(1)}} \tag{6}$$

or from a variance of it in case of gate-selected spectra, as described in [22]. In the previous expression N_{eve}, μ_1 and μ_2 are the number of counts and the first and second statistical moments of a $4\hbar^2/\Im^{(2)} \times 4\hbar^2/\Im^{(2)}$ two-dimensional sector placed either along the ridge or the valley region of the γ–γ matrix, while the correction term $P^{(2)}/P^{(1)}$ takes into account the finite resolution of the detector system, as discussed in [14].

As a consequence of the previous argumentation, the large and small number of paths associated with the continuum and discrete parts of the rotational spectrum, respectively, are found to be related to small and large fluctuations in the number of counts of the recorded rotational spectrum. In particular, as shown in figure 16, spectra resulting from the ratio of the first and second statistical moments of the number of counts recorded in the experimental channels of γ–γ energy spectra display large fluctuations along the ridge structure (populated by the rotational decay along the few discrete paths close to the yrast line) and rather small fluctuations along the central valley, mostly populated by events associated with continuum paths, which distribute more smoothly in the γ–γ coincidence plane. This results in a much

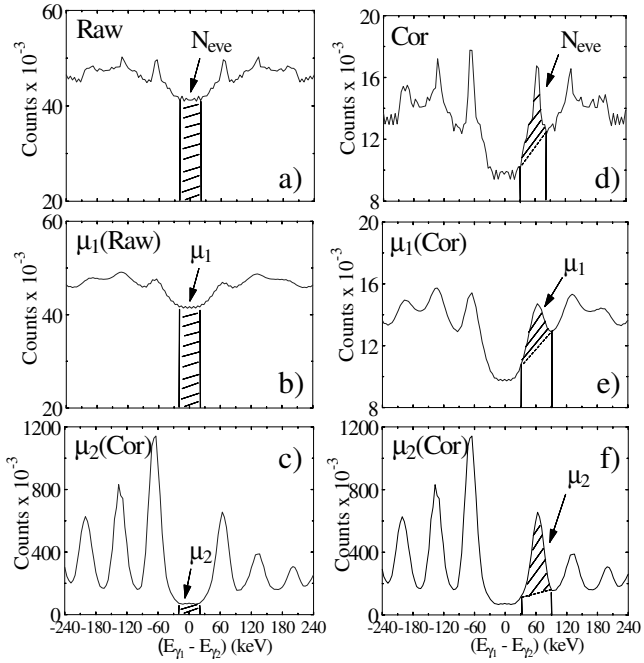

Figure 17. Example of perpendicular cuts on the γ–γ coincidence matrix of ^{168}Yb for the original (Raw), background subtracted (Cor) and statistical moment spectra distributions. The shaded regions indicate the integrated areas used to extracted the experimental number of paths, according to equation (6), both for the ridges (right) and for the valley (left) (adapted from [14]).

clearer ridge structure than in the original spectrum, making it easier to study the evolution of the rotational spectrum as a function of temperature [14].

The fluctuations of counts in each channel of the two-dimensional background subtracted spectra can be evaluated by the program STATFIT [14] and the corresponding statistical moments μ_1 and μ_2 stored into 2D spectra, after the spectra have been compressed to 4 keV/ch and all pairs of resolved transitions are removed from the matrices, by the Radware programs [46] (see figure 16). This ensures an exact evaluation of the fluctuations, which would otherwise be severely affected by the low lying intense transitions, as shown on the left-hand side of figure 16(*c*). Figures 17(*a*)–(*f*) show the relevant spectra used for the fluctuation analysis of the ridge and valley structures. In the figure, the spectral regions whose integral determines the number of paths through equation (6) are indicated by shaded areas.

It should be noticed that the limit of significance of the fluctuation analysis method is reached when each decay path is used only once, namely when there is no difference between distributing events over paths or directly over the experimental channels, therefore recovering the purely statistical limit. This situation can be especially encountered high up in the quasi-continuum, where at a given spin each rotational cascade can choose among an extremely large number of available transitions. Therefore, a meaningful fluctuation analysis of both ridge and valley structure of γ–γ coincidence spectra requires high counting statistics in each recorded channel, in order to be able to move away from the pure statistical limit. This is illustrated in figure 18, in the case of the fluctuation analysis of the valley region of ^{164}Yb [22]. As one can see, $\approx$1000 counts have to be collected in a 4 keV resolution channel of the background subtracted matrix (panel (*a*)) in order to obtain a measure of the fluctuations significantly larger than 1, which represent the purely statistical limit (full curve in figure 18(*b*)).

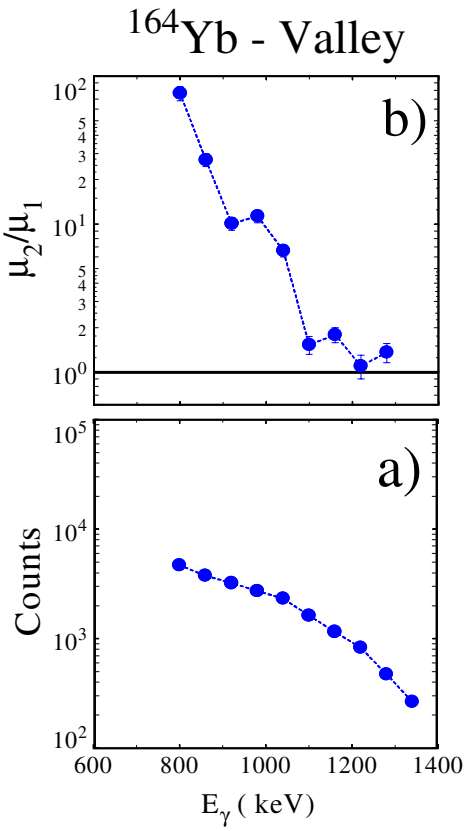

Figure 18. The number of counts collected in a 4 keV × 4 keV channel along the valley region of a 2D background subtracted spectrum of ^{164}Yb are shown in panel (*a*). The corresponding μ_2/μ_1 fluctuations are given in panel (*b*). The full curve represents the statistical limit obtained in the case of pure count fluctuations (adapted from [22]).

As will be discussed in section 6, the first main result obtained by comparing the experimental number of decay paths with predictions based on cranked shell model calculations, as for the ones discussed in section 3.1, is the experimental evidence for damping of rotational motion [13,15], together with rather detailed information on the two-body residual interaction playing such an important role at finite temperature.

Furthermore, as discussed in [21, 22], the study of the counts fluctuations in terms of covariance between pairs of γ–γ coincidence spectra allows us to investigate the similarity between different distributions of events. In particular, the covariance analysis has been used to study relevant physical properties of warm nuclei, like the degree of collectivity of the thermal rotation (see section 5) and the conservation of the quantum numbers with excitation energy (see section 7).

Figure 19 shows the main idea behind the covariance analysis, taking as an example the transition energy region (800, 900) keV × (700, 800) keV of two γ–γ coincidence matrices of an experiment on ^{164}Yb, with γ-rays emitted by recoiling nuclei in a Pb target backing [21]. In this case the matrices, called $M(A)$ and $M(B)$, are born asymmetric, having on the x and y axes the γ-ray energies detected at forward and backward angles (top part) and *vice versa* (middle panel). In the bottom part of the figure, the covariance of counts between the two previous distributions is shown, being evaluated according to the expression

$$\mu_{2,\mathrm{cov}}(A, B) \equiv \frac{1}{N_{ch}} \sum_j (M_j - \langle M_j \rangle) \times (N_j - \langle N_j \rangle). \tag{7}$$

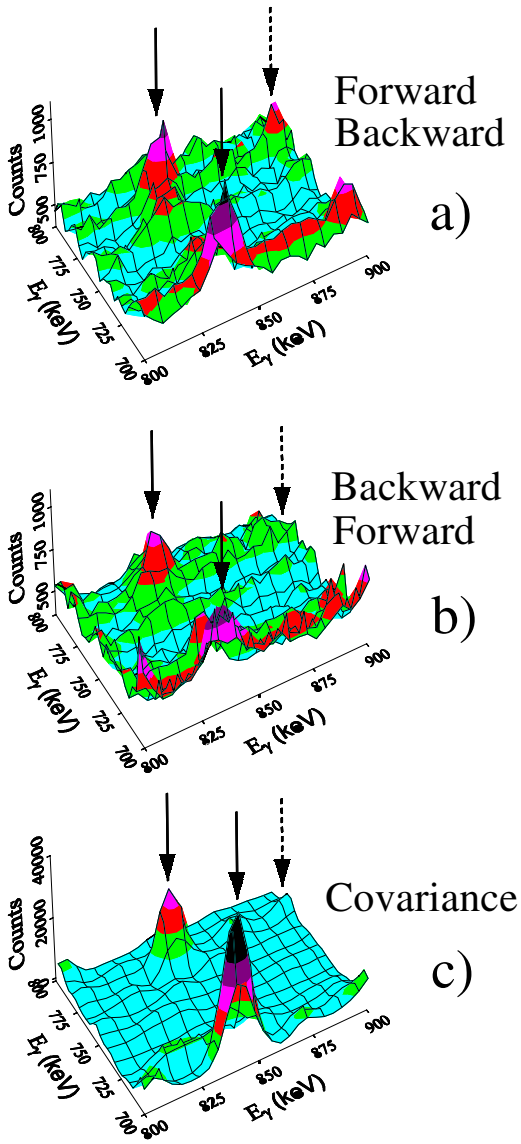

Figure 19. Sections of 2D coincidence matrices having on the x and y axes the γ-ray energies detected at forward and backward angles (a), and *vice versa* (b), in a backed target experiment on ^{164}Yb [21]. The covariance spectrum between the two previous distributions, defined according to equation (7), is shown in panel (c). The arrows indicate structures which are common (full) or not (broken) to the (a) and (b) distributions.

Here, the sum is over a region spanning N_{ch} channels in the 2D sector, while M_j and N_j are the number of counts in channel j of the two spectra and $\langle M_j \rangle$ and $\langle N_j \rangle$ denote local average spectra, which can be found by the program STATFIT [14] as a numerical smoothed third-order approximation of the 2D spectrum.

As one can see in figure 19(c), structures which are present in both the original spectra, indicated by full arrows, are further magnified in the covariance spectrum as compared to the surrounding background. This is not the case for structures appearing in only one of the two

matrices (indicated by broken arrows in the figure), which in the covariance spectrum become depressed.

As a consequence of this, one can imagine investigating in detail the similarity between two different distributions of counts, even when rather smooth and featureless, as for example the central valley of γ–γ coincidence spectra (see sections 5 and 7). In fact, one can normalize the covariance and establish the degree of correlation between two spectra by calculating the correlation coefficient $r(A, B)$ which measures directly how the spectrum $M(A)$ is similar to the spectrum $M(B)$. The coefficient $r(A, B)$ is defined as

$$r(A, B) \equiv \frac{\mu_{2,\mathrm{cov}}(A, B)}{\sqrt{(\mu_2(A) - \mu_1(A))(\mu_2(B) - \mu_1(B))}}. \tag{8}$$

Here, μ_1 and μ_2 denote the first and second statistical moments defined for the same region N_{ch}. In particular, μ_2 is related to the expression for the covariance by $\mu_2(A) = \mu_{2,\mathrm{cov}}(A, A)$. The subtraction of the first moments in the denominator of (8) corrects for the contribution to μ_2 from counting statistics, which is linear in the number of counts.

From the previous expression one finds that the correlation coefficient r becomes 1 for identical $M(A)$ and $M(B)$ distributions, while it is small and close to 0 for spectra having almost no features in common. This can be used to determine the similarity between pairs of γ–γ coincidence spectra, for example along the ridge and valley regions of the spectral distribution. In sections 5 and 7, results concerning the quadrupole deformation of the rotational quasi-continuum and the conservation of the quantum numbers in the excited rotating nucleus, obtained with this method, are discussed.

5. Lifetime measurements of the quasi-continuum

One of the basic assumptions on which the rotational damping model is based is that the nucleus rotates collectively, keeping the same quadrupole deformation of the cold rotational bands, even in the high excitation energy region where the damping mechanism dominates strongly. This has been assumed both in the original schematic picture formulated in [8] and also in the microscopic band mixing calculations described in section 3.1, which are performed at fixed deformation. Therefore, it becomes crucial to establish experimentally the degree of collectivity of the thermal rotation in order to give strong support not only to the rotational damping model, but also to its conclusions. This has been done by measuring the lifetimes of the rotational transitions as a function of excitation energy, both for the cold discrete excited rotational bands and for the mixed rotational transitions higher up in the quasi-continuum region [21, 23].

Figure 20 schematically shows the different methods used to determine experimentally the lifetimes of rotational transitions in the different temperature regions, taking as an example a two-dimensional matrix collecting the γ-ray contributions from a backed target experiment on ^{164}Yb at forward–backward angles [21]. In the case of discrete transitions belonging to low-lying bands the lifetimes analysis is based on the study of the Doppler shift of the peak position at forward and backward angles. This can be obtained, for example, by projecting on the x and y axes the forward–backward γ–γ coincidence matrix, as schematically illustrated in figure 20(b) for the 889.2 keV yrast transition of ^{164}Yb.

Concerning the unresolved transitions of regular excited rotational bands forming the ridge structure in $E_{\gamma_1} \times E_{\gamma_2}$ spectra, the lifetime analysis is based on the study of the Doppler shift of the ridges in the forward–backward and backward–forward γ–γ matrices, as schematically illustrated in figures 20(a) and (c). After subtracting the background by means of the COR procedure [4], two sets of spectra are obtained from wide cuts perpendicular to the $E_{\gamma_1} = E_{\gamma_2}$

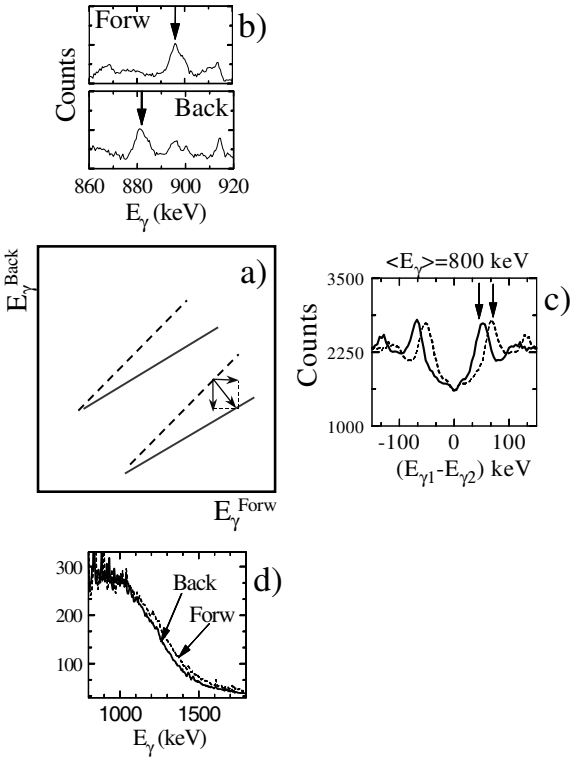

Figure 20. Illustration of the Doppler shift attenuation techniques employed in the study of the lifetimes of the rotational structures corresponding to different regions of excitation energy, making use, as an example, of a 2D coincidence matrix of ^{164}Yb [21]. Panel (*a*) schematically illustrates a γ–γ matrix: the broken lines indicate the position of the ridge structure in the symmetric matrix, while the full lines show the corresponding position in a forward–backward matrix, as a consequence of the Doppler shift (indicated by arrows). Panel (*b*) shows the shift at forward and backward angles of the 889.2 keV yrast transition of ^{164}Yb; the spectra can be obtained by projecting on the x and y axes the 2D matrix. The Doppler shift of the discrete excited rotational bands can be deduced from the shift of the ridge structure observed in perpendicular cuts of the forward–backward and backward–forward spectra, as shown in panel (*c*) for the average transition energy $\langle E_\gamma \rangle = 800$ keV. The Doppler shift of the E2 bump, collecting intensity from damped rotational transitions, can be deduced from the analysis of 1D spectra at forward and backward angles (obtained by projecting the γ–γ matrix on the x and y axes), as shown in panel (*d*).

diagonal of the two matrices. This is shown in figure 20(*c*) for the average transition energy $\langle E_\gamma \rangle = 800$ keV. As one can see, the amount of shift of the ridge structure can clearly be seen (as pointed out by arrows), allowing for a precise determination of the effective quadrupole moment of the discrete excited rotational bands, as discussed later in connection with figure 24.

The simplest and most direct way to measure lifetimes of transitions in the damped region is to deduce the fractional Doppler shift from 1D spectra at forward and backward angles in the energy region where the spectral shape changes, namely the upper edge of the E2 continuous bump. The 1D spectra can be obtained, for example, by projecting on the x and y axes the forward–backward matrix, as shown in figure 20(*d*). The size of the shift of the E2 bump, which in the case of ^{164}Yb can be clearly observed only in the energy interval $1200 < E_\gamma < 1400$ keV, can then be obtained by the procedure described in [23]. Since these high energy transitions of the E2 bump are often fully shifted, it is not possible from such simple analysis to obtain a

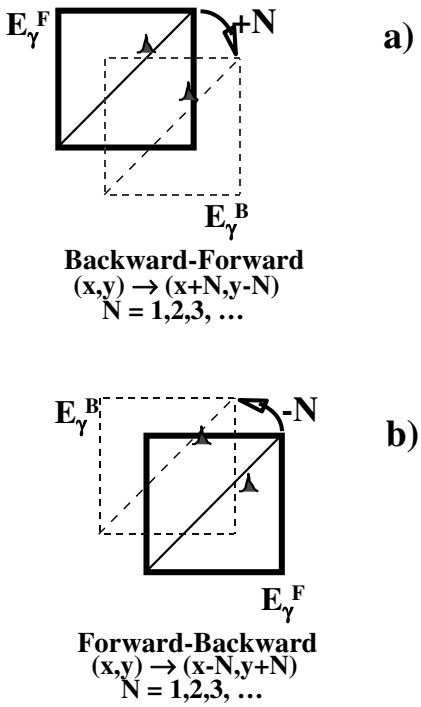

Figure 21. Schematic illustration of the construction of pairs of backward–forward (*a*) and forward–backward (*b*) matrices, obtained by shifting the counts in channel (x, y) to $(x-N, y+N)$ and $(x + N, y - N)$ with $N = 1, 2, 3, \ldots$, respectively. By studying the covariance between the two sets of spectra one can determine the Doppler shift of the $E_{\gamma_1} = E_{\gamma_2}$ valley region, as discussed in the text.

defined value for the quadrupole moment, but only an upper limit of $\approx 10^{-14}$ s for the effective feeding plus lifetimes of the rotational states in the quasi-continuum.

As a consequence of the lifetime analysis of the E2 bump, to obtain a more definite measurement of the nuclear quadrupole moment of the strongly mixed bands one has to focus on lower transition energies, where the values of the fractional shifts are expected to be smaller than 1. This cannot be done by studying the shift in 1D spectra because at lower transition energies the 1D E2 bump is flat with superposed contributions from discrete regular bands (see figure 20(*d*)). In contrast, one can study the valley structure of the $E_{\gamma_1} \times E_{\gamma_2}$ spectrum, which is mainly populated by damped rotational transitions and almost free of regular rotational bands. Since this region of the spectrum is also flat and continuous, the amount of the shift cannot be easily extracted from a direct inspection of the spectrum landscape in forward–backward and backward–forward matrices, as one can see in figure 20(*c*). Therefore, a more sensitive method has been developed to extract the Doppler shift of the valley region, based on the covariance analysis of the fluctuations of counts in pairs of 2D spectra (see section 4) [21]. The general idea behind the method consists in comparing the valley regions of forward–backward and backward–forward matrices shifted relative to each other, until the maximum overlap between the two distributions is found. In this situation, the displacement between the two matrices will give the Doppler shift of the damped rotational transitions populating the valley region of the spectrum. For this purpose, as described in [21], the data are sorted into 2D spectra, namely $(E^F_{\gamma_1} \times E^B_{\gamma_2})$ and $(E^B_{\gamma_1} \times E^F_{\gamma_2})$, where B and F indicate backward and forward angles, respectively. Two sets of spectra are then constructed. The first consists of spectra of the type $(E^B_{\gamma_1} \times E^F_{\gamma_2})_{\mathrm{Shift}=N}$, obtained by shifting the counts in channel (X, Y) to channel $(X+N, Y-N)$, each corresponding to given integer values, $N = 1, 2, 3, \ldots$, as schematically illustrated in figure 21(*a*). The second set consists of spectra of the type $(E^F_{\gamma_1} \times E^B_{\gamma_2})_{\mathrm{Shift}=-N}$, obtained by shifting the counts in channel (X, Y) to channel $(X - N, Y + N)$, as shown in figure 21(*b*).

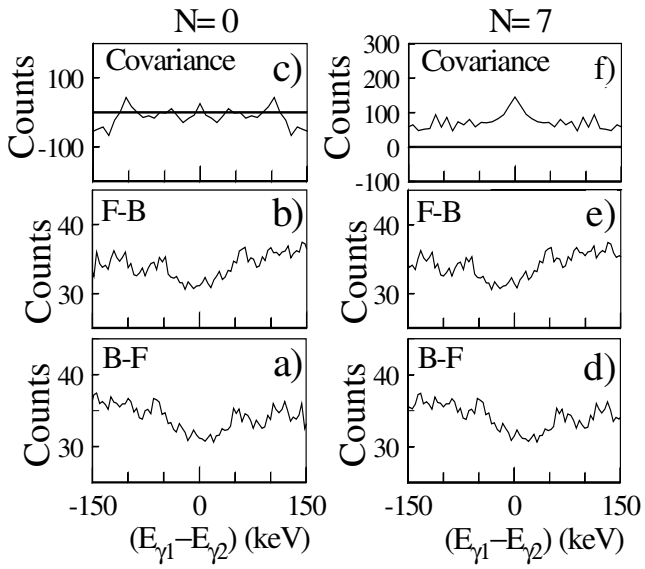

Figure 22. Perpendicular cuts on the original backward–forward (*a*), forward–backward (*b*) and corresponding covariance (*c*) spectra of ^{164}Yb. The same cuts are shown in panel (*d*), (*e*) and (*f*) for the pairs of spectra relatively shifted by $N = 7$ channels, as schematically illustrated in figure 21 (adapted from [47]).

The correlations in fluctuations between any two $(E^B_{\gamma_1} \times E^F_{\gamma_2})_{\text{Shift}=N}$ and $(E^F_{\gamma_1} \times E^B_{\gamma_2})_{\text{Shift}=-N}$ spectra are then evaluated in terms of the covariance of counts, defined according to equation (7). Figure 22 shows, as an example, two perpendicular cuts at $\langle E_\gamma \rangle = 960$ keV on the matrices $(E^B_{\gamma_1} \times E^F_{\gamma_2})$ and $(E^F_{\gamma_1} \times E^B_{\gamma_2})$ with no shift (parts (*a*) and (*b*)) and on the matrices $(E^B_{\gamma_1} \times E^F_{\gamma_2})_{\text{Shift}=-14\text{ keV}}$ and $(E^F_{\gamma_1} \times E^B_{\gamma_2})_{\text{Shift}=14\text{ keV}}$ with a relative shift of 28 keV (parts (*d*) and (*e*)). As shown in the corresponding top panels, the covariance spectrum in the valley region is small ($\approx$0, see part (*c*)) before we shift the matrices relative to each other, while it has a large value (part (*f*)) when in this case the relative shift is 28 keV.

The degree of correlation between the two spectra is then determined by the correlation coefficient r defined according to equation (8). Figure 23 shows a typical example of the correlation coefficient r as a function of the relative shifts between the forward–backward and backward–forward matrices for the transition energy $\langle E_\gamma \rangle = 880, 920$ and 1000 keV. The arrows on the figure indicate the values corresponding to the maximum of the correlation coefficient r and to the full shift position, from which one can deduce the fractional Doppler shift $F(\tau)$. In the present case, the covariance analysis of the valley shows that, in the $800 < E_\gamma < 1000$ keV region, the fractional Doppler shift $F(\tau)$ is significantly smaller than 1, therefore providing a definite value for the quadrupole moment.

The experimental results obtained for the fractional Doppler shift $F(\tau)$ of the nucleus ^{164}Yb in the different excitation energy region of the spectrum are summarized in figure 24. As can be seen in the figure, $F(\tau)$ displays a smooth increase with $\langle E_\gamma \rangle$, and consistency is found among the Doppler shift analysis of the different regions of the γ–γ spectrum.

The measured fractional Doppler shifts shown in figure 24 correspond to the effective decay times related to the history of the paths from the entry point to the time of emission of the observed transitions. Therefore, in order to extract the nuclear quadrupole moment Q_t from the measured shifts, the γ cascades from the excited nucleus have to be realistically simulated, starting from an entry distribution in energy and spin of the residual nucleus and ending at the

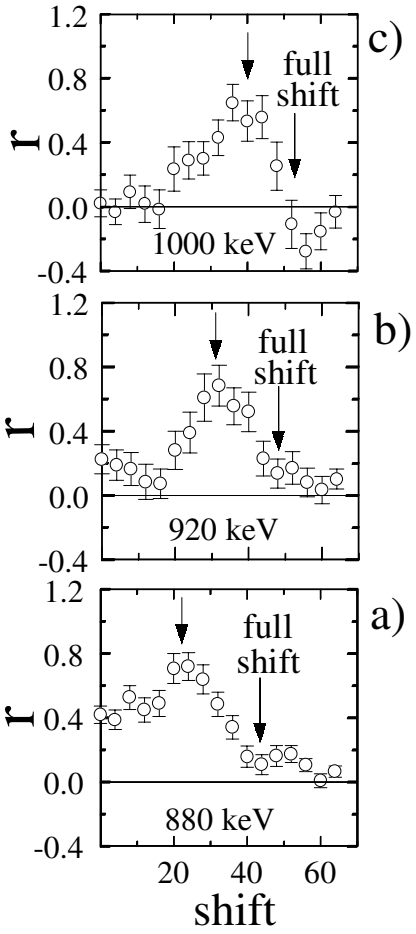

Figure 23. The correlation coefficient r, defined by equation (8), obtained from the covariance analysis of the valley region as a function of the relative shift between pairs of backward–forward and forward–backward matrices, is shown for the average transition energies $\langle E_\gamma \rangle = 880, 920$ and 1000 keV. The arrows indicate the values of the shifts corresponding to the maximum of r and the full shift (adapted from [47]).

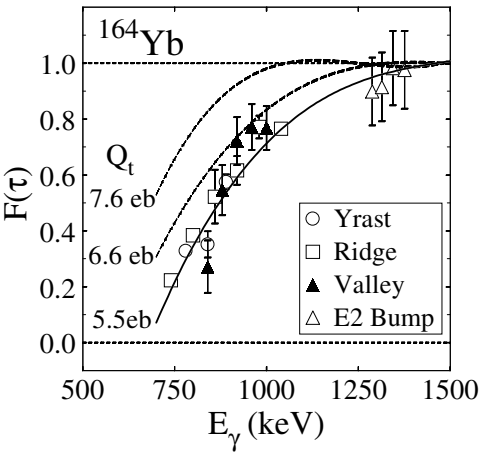

Figure 24. The measured fractional Doppler shift for some discrete transitions and for different parts of the quasi-continuum spectrum of ^{164}Yb. The curves represent the expected theoretical values for $Q_t = 5.5, 6.6$ and 7.7 eb (corresponding to 200, 300 and 400 Weisskopf units, respectively), as obtained from simulated spectra (adapted from [21]).

transition in question. For this purpose the simulation code MONTESTELLA [15], briefly discussed in section 3.2, has been employed and the intrinsic lifetime τ_i of a state i at spin I

and excitation energy U_i was calculated starting from the transition probabilities for E1 and E2 decay $T(\mathrm{E1}, U_i)$ and $T(\mathrm{E2}, U_i)$ as

$$\tau_i(I) = \frac{1}{T(\mathrm{E1}, U_i) + T(\mathrm{E2}, U_i)}. \tag{9}$$

The simulation program calculates the effective lifetime τ of a transition at spin I as the sum of the lifetimes τ_i of the preceding transitions with spin $J \geqslant I$, $\tau(I) = \Sigma_{J \geqslant I} \tau_i(J)$. Making use of the velocity profile of the recoiling nucleus in the target and backing [48–50] the program calculates the velocity of the nucleus at time τ and then the associated Doppler shift of the γ transition energy.

The fractional shifts deduced from simulated spectra of ^{168}Yb, taken as a representative ND nucleus of the rare earth region ($\epsilon_2 \approx 0.25$), are shown in figure 24 by lines for the three different values of $Q_t = 5.5$, 6.6 and 7.6 eb, in comparison with the experimental results. As one can see, the data are well described over the entire transition energy range by the curve corresponding to the quadrupole moment $Q_t = 5.5$ b (or 200 Wu), for all the experimental observables.

On the basis of the lifetimes analysis presented here one can then draw an important conclusion: not only the discrete excited bands, giving rise to ridge structures in γ–γ matrices, carry the same rotational collectivity as the yrast band, but this collectivity is also maintained by the thermally excited mixed bands, filling the valley region of the 2D spectra, and extending up to about 2 MeV of excitation energy above yrast. This is the excitation energy region where the major part of the γ cascades goes, as shown in figure 11, and where the damping of rotational motion is expected to play a major role. One can conclude that the lifetime analysis of the excited rotational motion in the rare earth nucleus ^{164}Yb verifies the basic assumption of the rotational damping model.

6. Role of the residual interaction: evidence for rotational damping

The new generation of γ-detector arrays has made it possible to study in great detail the properties of the nuclear motion at high rotational frequencies as well as in a variety of nuclear shapes and deformations. In the best studied cases [51, 52] up to 30 discrete rotational bands have been resolved and well described within the framework of the cranked mean field [25]. At the lowest temperatures, occasional interactions at the crossing between bands start to be observed, being in most cases interpreted as a perturbation of the mean field description. In particular, the splitting of the rotational strength occurring at the crossings can be considered as a precursor of the fragmentation of the rotational decay, which is expected to dominate strongly at higher excitation energies. In fact, with increasing heat energy the average spacing between rotational bands decreases rapidly, so that, in a rare earth nucleus, already at 1 MeV of excitation energy above yrast interactions and crossover transitions are expected to be a rule more than an exception. In this respect, it becomes crucial to investigate the role played by the residual interaction in the description of the nuclear system at finite temperature.

As discussed in section 3 in connection with the band mixing model, the experimental study of the damping of rotational motion can be instrumental for shedding light on the properties of the nuclear many-body systems beyond the mean field description. In fact, quantitative studies of quasi-continuum rotational spectra, in terms of variance and covariance of the recorded counts (see section 4), can be used to obtain information on the kind and magnitude of the two-body interaction governing the mixing among rotational bands.

Figure 25 shows the experimental results of the fluctuation analysis [14] of the ridge–valley structure of a γ–γ coincidence matrix of ^{168}Yb, in comparison with predictions from

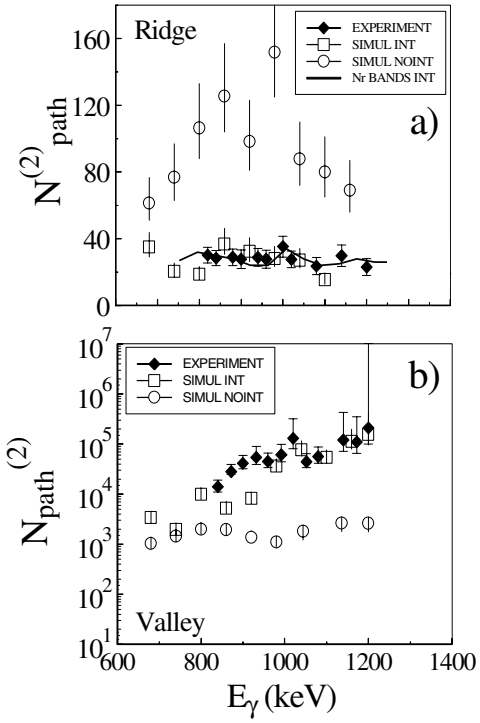

Figure 25. The effective number of paths $N^{(2)}_{\rm path}$ extracted from the fluctuation analysis of the ridge (*a*) and valley (*b*) structure of ^{168}Yb in comparison with predicted values from band mixing calculations [10]. The full diamonds correspond to the data, the open squares to simulations based on mixed bands, and the open circles to simulations based on non-interacting bands. The full curve in panel (*a*) gives the number of discrete bands calculated with the conditions $n_{\rm branch} \leqslant 2$ [15].

band mixing calculations [10, 15]. The analysis is focused on the importance of the residual interaction in the description of the warm rotation. As shown in panel (*a*), a total number of $\approx$30 paths is obtained from the fluctuation analysis of the first ridge of the matrix selecting the entire decay flow of the nucleus (full symbols). This is in agreement with systematic results obtained for a variety of nuclei of the same mass region and deformation [14]. The result is well reproduced by the calculated number of paths, as extracted from the band mixing model with the requirement $n_{\rm branch} < 2$ (full curve in panel (*a*)) [10], and it also agrees with the number of paths extracted from the simulated ridge (open squares in figure 25(*a*)) obtained by the MONTESTELLA code based on mixed band calculations with standard interaction strength $V_0 = 27.5$ MeV/A (see section 3.2). This strongly supports the interpretation that the ridge structures experimentally observed in γ–γ matrices are mostly populated by regular rotational bands, as discussed in sections 2 and 4. In addition, the comparison with the band mixing model indicates that, in a typical ND nucleus of the rare earth region, the regular rotational motion along discrete bands is expected to survive up to $\approx$1 MeV excitation energy above yrast, before rotational damping sets in.

The fluctuation analysis of the valley region, collecting intensity from the warmer region of damped rotation, gives instead a large number of paths, of the order of 10^4, as shown in figure 25(*b*). This is also in agreement with the study of other nuclei of the same mass region and deformation [14, 53], and with the number of paths from simulated γ–γ coincidence spectra based on microscopic band mixing calculations (square symbols in panel (*b*)). In contrast, the fluctuation analysis of simulated spectra based on pure cranked shell model bands (e.g. *not* mixed) gives a number of paths either much larger, as in the case of the ridges (open circles in panel (*a*)), or much smaller, as in the case of the valley (open circles in panel (*b*)) in strong disagreement with the experimental data.

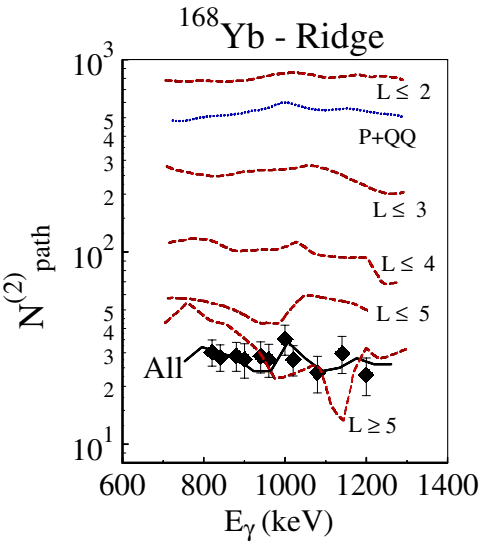

Figure 26. The effective number of paths $N^{(2)}_{path}$ extracted from the fluctuation analysis of the ridge structure of ^{168}Yb (full diamonds) in comparison with the predicted values from band mixing calculations for various multiple decompositions of the SDI residual interaction (broken curves labelled by L). The calculation including all multiples is shown by the full curve (the same as in figure 25). The number of paths calculated with the pairing plus quadrupole force (P + QQ) is also plotted as the dotted curve (adapted from [10]).

One can then conclude that the overall agreement between data and band mixing calculations gives the *first experimental evidence of rotational damping*, namely of the fragmentation of the rotational decay induced by the two-body residual interaction [13], giving strong support to the validity of the band mixing model discussed in section 3.

The fluctuation analysis of the ridge structure can be further employed to test the sensitivity to the type and strength of the two-body residual interaction. As shown in figure 26, the predicted values for the number of discrete rotational bands strongly depends on the number of multiples included in the SDI force. In particular, several hundred rotational bands are found for a low multiple ($L \leqslant 3$) SDI force as well as for a pairing plus quadrupole (P + QQ) type of interaction, in strong disagreement with the experimental data (full diamonds). On the other hand, high multiple components ($L \geqslant 5$) of the SDI force are found to give essentially the same number of rotational bands as the full multiple SDI, indicating that the onset of rotational damping mostly originates from the high multiple terms of the two-body residual interaction. This can be related to the fact that both the P + QQ and the low multiple SDI forces usually have strong selectivity or selection rules on the quantum numbers of the intrinsic configurations, therefore inducing a less effective mixing between the nuclear states. In addition, as discussed in section 3 in connection with figure 10, with increasing heat energy the full SDI force is found to produce a transition from regular motion to quantum chaos at variance from the P + QQ interaction, therefore providing a better description of the nuclear system on its way to the compound nucleus regime.

Once the nature of the two-body-force is established, the sensitivity to the strength of the residual interaction still remains to be tested. For discrete rotational bands close to the yrast line, the magnitude of the interaction matrix element can be experimentally determined from the intensities of the crossover transitions occasionally observed between the bands and the value of the energy repulsion, according to the method described in [54]. In the case of the rare earth nuclei ^{162}Tm, ^{163}Tm, ^{163}Er and ^{164}Lu, 19 two-body crossings have been identified, with an average interaction strength

$$\sqrt{\langle |V|^2 \rangle_{\rm exp}} = 14 \text{ keV} \tag{10}$$

as shown in figure 27 [55]. As one can see, large variations in the absolute value of the

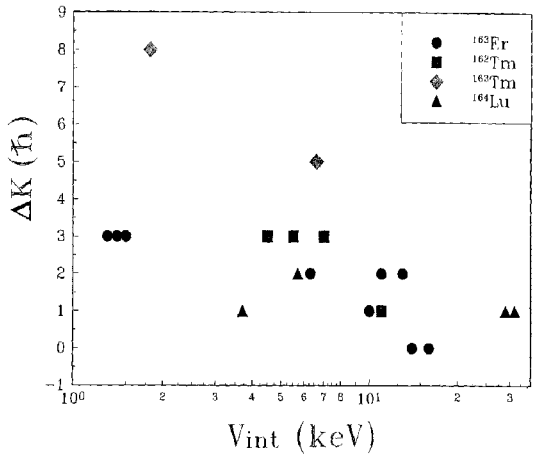

Figure 27. The absolute value of the interaction matrix elements of two-body nature, experimentally measured at the band crossings for a number of rare earth nuclei, is related to the difference in the K quantum number between the configurations of the interacting bands (adapted from [55]).

interaction strength are observed, depending on the difference in the K quantum number between the configurations of the interacting bands. In particular, large changes in K are found to be generally associated with small interactions, pointing to a less effective mixing between intrinsic configurations characterized by very different K quantum numbers, as will also be discussed in section 7.

In the case of the warm rotation, the sensitivity to the strength of the residual interaction can be tested by applying the fluctuation analysis to the ridge structures observed in the γ–γ matrix and in the *tilted rotational planes* of a triple γ coincident matrix, defined by equation (2) in section 2.3. In fact, making use of the enhanced experimental sensitivity to the ridge structures formed by unresolved regular rotational cascades in the 3D spectrum (see figure 4), it is possible to determine experimentally the number of regular rotational paths 2 or more steps long [32].

As discussed in [32] in the case of ^{168}Yb, the analysis of the ridge structure of the tilted rotational planes gives a fewer number of regular rotational bands when the length of the cascade is increased, as a consequence of the fragmentation of the E2 strength which destroys the rotational energy correlations expressed by equation (2). This can be used to determine the strength of the two-body residual interaction, as shown in figure 28, where the average number of paths are given as a function of the cascade length, for both data and calculations with different interaction strengths. As one can see, the band mixing calculations are found to reproduce well the experimental number of discrete bands 2, 3, 4 and 5 steps long for an effective two-body residual interaction of surface delta type, with standard strength $V_0 = 27.5/A$ MeV (full curve in the figure) [10]. This corresponds to an average strength of the two-body matrix elements

$$\sqrt{\langle |V|^2 \rangle_{\mathrm{SDI}}} = 20 \text{ keV} \tag{11}$$

which is not too far from the 14 keV value previously obtained from the band mixing analysis of the discrete bands, as shown in figure 27. In addition, figure 28 shows strong disagreement between data and calculations when the strength of the residual interactions is either increased or reduced by a factor of 2.

In conclusion, the experimental and theoretical findings discussed in this section definitely demonstrate the crucial role played by the residual interaction in the description of the warm

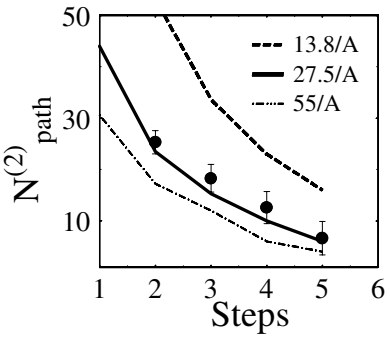

Figure 28. The average number of bands obtained from the experimental analysis of the measured 2D and 3D ridge structures of ^{168}Yb as a function of the number of decay steps (points), in comparison with the predictions from cranked shell model calculations plus a two-body residual interaction with interaction strength $V_0 = 13.8/A$, $27.5/A$ and $55/A$ MeV (curves) [32].

rotation. In particular, evidence for the damping of rotational motion is found, and its origin is related to the high-multiple terms of the residual two-body interaction, which are also responsible for the onset of chaos at higher excitation energies. In addition, the magnitude of the interaction strength deduced from the analysis of quasi-continuum rotational spectra is found to be consistent with the experimental value obtained from the zero-temperature region.

7. Configuration dependence of band mixing

Having established experimentally the crucial role played by the residual interaction in the damping mechanism, as discussed in section 6, further insight into the band mixing process requires exclusive studies based on a selection of the nuclear configuration. This can probe in more detail the properties of the residual interaction. In particular, by focusing on the analysis of unresolved rotational transitions feeding low-lying configurations of the nuclear system, one can test the dependence of the two-body residual force on the different quantum numbers (signature, $K, \ldots$) of the intrinsic configuration, namely the dependence of rotational damping on the nuclear configuration.

For this purpose, in the present section we will mainly discuss the results of the fluctuation analysis on two ND nuclei of the rare earth region ^{164}Yb and ^{163}Er [22, 53], the latter being especially interesting due to the presence of high K rotational structures, besides the more frequently observed low K ones [51].

The results of the fluctuation analysis of γ–γ coincidence matrices of ^{164}Yb and ^{163}Er [22, 53] are shown in figure 29. In both cases the data have been sorted into a number of spectra collecting either the entire decay flow of the reaction channel (total matrices) or selecting specific intrinsic nuclear configurations.

In the case of ^{164}Yb, the analysis of the ridge structure of the total matrix gives $\approx$25 discrete regular bands (full circles in panel (*a*)), in good agreement with systematic results obtained for a variety of nuclei of the same mass region and deformation [14] (as shown, for example, in figure 25), and with the band mixing predictions (full curve) [10]. In addition, an average number of paths $\approx$10, fairly independent of the γ-ray energy and with no appreciable difference among the specific configurations, is obtained from the analysis of the ridges of matrices gated by the signature and parity configurations $(\alpha, \pi) = (0, +)$, $(0, -)$ and $(1, -)$ (open circles in panel (*a*)). This latter quantity measures the effective number of discrete paths which eventually will feed into a given (α, π) gate-selected band. Again, even in this more selective case, good agreement is observed between data and band mixing calculations (broken curve). As will be discussed in section 8 in connection with the covariance analysis of the gate-selected spectra, the fact that the sum of the number of paths gated by specific

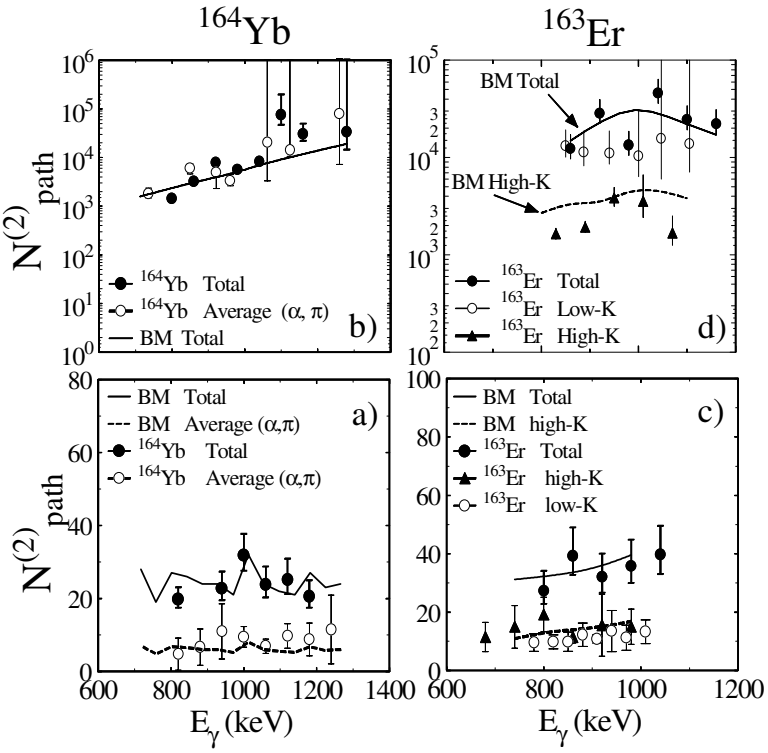

Figure 29. The number of paths $N^{(2)}_{\rm path}$ extracted from the fluctuation analysis of the ridge and valley structures gated on specific configurations of ^{164}Yb and ^{163}Er nuclei, left and right respectively. In both cases the full circles refer to the analysis of the total γ–γ matrices, collecting the entire decay flow of the specific nucleus, while the open symbols correspond to the average values obtained from the study of 2D spectra gated by the intrinsic (α, π) configurations with low values of the K quantum number. In the case of ^{163}Er the closed triangles give the average number of paths extracted from the fluctuation analysis of ridge (c) and valley (d) structures of γ–γ matrices gated by high K bands. The curves in the figures have been obtained from cranked shell model calculations including a two-body residual interaction of surface delta type [10] (adapted from [22, 53]).

configurations is higher than the value obtained from the analysis of the total matrix suggests that the γ cascades selected by different gates have some common paths.

The fluctuation analysis of the valley region (panel (b)) gives, instead, a large number of paths, of the order of 10^4, for both the total and the (α,π) gate-selected matrices, in agreement with similar studies on neighbouring nuclei [14] (see section 6). This is also in agreement with simulation calculations based on the microscopic band mixing model (see section 3), supporting the assumption of rotational damping.

A similar fluctuation analysis has been performed on the 2D matrices of ^{163}Er, as shown in figures 29(c) and (d). In this case a total number of $\approx$35 discrete regular bands (full circles) is obtained from the ridge analysis of the total matrix (panel (c)), in agreement with the microscopic band mixing calculations for the specific case, while about 10 and 15 unresolved bands are found on average from the analysis of the 2D matrices gated by low K (open circles) and high K (full triangles) intrinsic structures, respectively, also in agreement with the band mixing predictions (broken curve). Even in this case, as previously observed for the nucleus ^{164}Yb, the sum of the gated results is different than the value obtained from the analysis of the ridge structure of the total matrix, suggesting that some γ cascades will have common decay

paths, giving non-zero covariance. In the case of ^{163}Er, in contrast to the results of the ridge analysis, the number of paths obtained from the valley region is found to depend significantly on the nuclear configuration. This is shown in figure 29(d) together with the number of paths deduced from the total $E_{\gamma 1} \times E_{\gamma 2}$ spectrum. As in the case of ^{164}Yb, a number of paths of the order of $\approx 10^4$ is found for both the total spectrum and the low K gated matrices, in agreement with the simulation calculations for the specific nucleus [15]. In contrast, the number of paths obtained from the valley of spectra gated by high K bands is found to be about five times smaller and well reproduced by the model predictions (broken curve). As a possible explanation it has been proposed that high and low K states do not mix together in the region of unresolved transitions [53]. This is consistent with the small value of the interaction strength measured for specific interacting bands with large differences in the K quantum numbers, as shown in figure 27. In addition, the smaller number of paths observed in the valley region of high K gated matrices also suggests that a reduced mixing may take place in the region of high K bands.

As a final comment on the analysis, one should notice that the large error bars obtained at high transition energies for the fluctuation analysis of the valley region are a consequence of two possible different effects: (i) the weakening of the E2 continuum in favour of E1 statistical transitions, as shown by the 1D spectra of ^{164}Yb in figure 1; and (ii) the poor counting statistics collected in the valley region of the 2D gated matrices. In fact, as shown in figure 18 in connection with the ^{164}Yb experiment, a typical low resolution channel (4 keV/ch) of the background subtracted matrix contains at most a few hundred counts in the high transition energy region ($E_\gamma \geqslant 1$ MeV). This makes the statistical analysis of the valley very difficult, as demonstrated by the corresponding μ_2/μ_1 ratio shown in the top part of the figure. In fact, for $E_\gamma \geqslant 1$ MeV the normalized fluctuations gradually approach 1 (full line), which is the statistical limit obtained in the case of pure count fluctuations [14].

8. Conservation of the K quantum number

The study of the count fluctuations of 2D spectra, as discussed so far, has allowed us to investigate the average properties of the rotational motion built on specific nuclear configurations. More detailed information, related for example to the validity of the selection rules for unresolved rotational bands, can be obtained by studying the covariance between spectra derived from different gating conditions. In fact, as briefly discussed in section 4, the covariance provides a measure of the similarity between different distributions of events: therefore, if applied to the ridge–valley structure of γ coincidence matrices, it can tell us about the similarity between the cascades feeding into different selected bands. This can in turn be related to the validity of the selection rules associated with the quantum numbers of the intrinsic nuclear structures.

In the following, we will concentrate the discussion on the projection K of the angular momentum on the nuclear symmetry axis, taking as an example the two ND nuclei of the rare earth region ^{164}Yb and ^{163}Er [22,53], previously investigated in connection with the fluctuation analysis of the ridge–valley structures of 2D matrices (see section 6). As discussed in [56,57], experimental and theoretical results indicate an incomplete mixing of the K quantum number for neutron resonance states, in contradiction with the expectation for a chaotic regime at the excitation energy region where these resonances occur [58]. In our case we will investigate a complementary problem, namely the persistence of the K quantum number for nuclear states at high rotational frequency and moderate excitation energy, e.g. $\approx$2 MeV, where the average γ-decay flow goes, as shown in figure 11.

Figure 30 shows the correlation coefficient r, defined according to equation (8), extracted from the analysis of the ridge structures for combinations of selected configurations of ^{164}Yb (panel (a)) and ^{163}Er (panel (b)). The lines at $r = 0$ and 1 correspond to the expected values

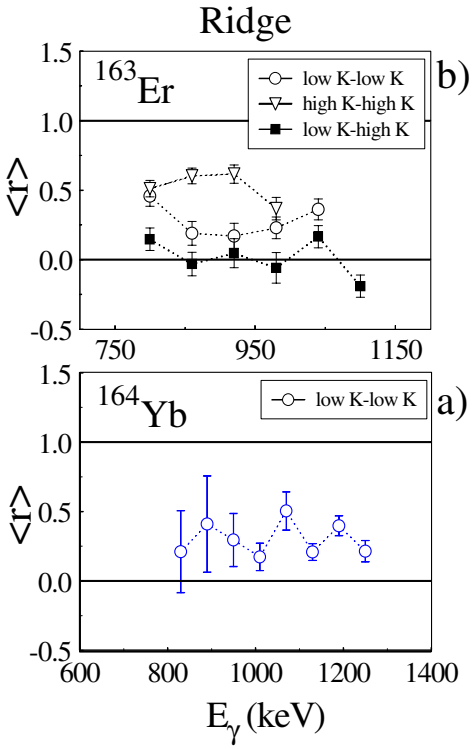

Figure 30. The average values of the correlation coefficient r extracted from the analysis of the ridge in ^{164}Yb and ^{163}Er nuclei, (*a*) and (*b*) respectively, as a function of the average transition energy. The open circles refer, in both cases, to the covariance analysis between pairs of spectra gated by intrinsic configurations with low values of the K quantum number. In the case of ^{163}Er, the correlation coefficient has also been extracted for combinations of 2D spectra gated by low K–high K (squares) and high K–high K (triangles) configurations. The line at $r = 0$ indicates decay paths completely decoupled, while the line at $r = 1$ indicates paths fully in common (adapted from [22, 53]).

of the correlation coefficient in the case of independent or identical decay paths. In particular, while the limit $r \to 0$ is expected to be reached when comparing the decay flows at $\approx$0 temperature, where the nuclear system is governed by strong selection rules, the opposite limit, $r \to 1$, is expected in a compound nucleus regime. In fact, for a compound nucleus at sufficiently high temperature, essentially only the parity and signature remain as good quantum numbers of the individual states [59], implying that any state at the compound level can democratically feed the various low-lying configurations, via complicated cascades containing varying numbers of E1 cooling transitions with different changes of signature.

As one can see from figure 30, for both nuclei the average value of the correlation coefficient r extracted from the analysis of the ridge structures is found positive for similar configurations (low K with low K, open circles, and high K with high K, open triangles) and of the order of 0.3–0.5, over the whole transition energy region. This result indicates that selection rules are important for the cascades among unmixed bands of similar intrinsic structures, being obeyed in roughly 70–50% of the parts of the cascades being investigated, and broken in the remaining 30–50%, for ^{164}Yb and ^{163}Er respectively. In contrast, in the case of ^{163}Er a cross-talk between low and high K bands is found to be hindered, as displayed by a correlation coefficient close to 0 (full squares in panel (*b*)) [53]. This result can be interpreted as an effect of the persistence of a strong K selection rule governing the excited rotational bands, at least until rotational damping set in. This means that the discrete excited bands are expected to behave not much differently than the low-lying configurations, for which the K quantum number plays an important role, as demonstrated by the small value of the strength of the residual interaction measured between low-lying interacting bands with large changes in K (see the discussion in section 6 in connection with figure 27).

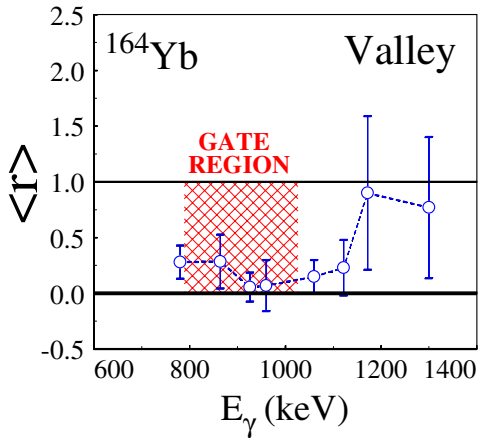

Figure 31. The average value of the correlation coefficient r, as obtained from the analysis of the valley region of pairs of γ–γ coincidence spectra of ^{164}Yb gated by the intrinsic (α, π) configurations with low values of the K quantum number. The shaded area indicates the transition energy interval covered by the gating transitions. In this case the line at $r = 1$ represents the compound nucleus limit (adapted from [22]).

The possible persistence of the K quantum number at moderate excitation energies was already suggested by the reduced number of paths obtained from the fluctuation analysis of the valley region of high K gated matrices of ^{163}Er, as compared with similar results for low K spectra (see section 7). If indeed K is conserved even at higher spins and internal energy, namely in the region of rotational damping, the reason is not yet understood, since the K quantum number is expected to be destroyed by the Coriolis force. In this respect, the covariance analysis may provide a general tool to address experimentally this question when many decay paths are available. As shown in figure 31, an attempt has been made for a covariance analysis of the valley region in the case of ^{164}Yb, an analysis which could not be performed for the ^{163}Er nucleus due to the limited statistics of the available data [53]. It is found that the correlation coefficient r is close to 0 in the transition energy region covered by the gate-selected γ-rays, while at higher transition energies r seems to assume large positive values, suggesting a stronger sharing of decay paths among cascades which finally feed into different intrinsic configurations, all characterized by low K quantum numbers. This can be taken as an indication of an approach to a compound situation for the part of the decay which lies at a heat energy $\geqslant$1 MeV, with rotational frequency between 500–650 keV, where the damping phenomenon dominates strongly. However, the most controversial issue, namely if a large difference in K survives in the region of rotational damping, still remains to be tested, requiring large statistics of data gated by intrinsic configurations with high value of the K quantum number, which are most often rather weakly populated.

9. Mass dependence of rotational damping

In the original formulation of the damping model [8], schematic estimates for the scaling of the mixing process of the mean field bands with the mass number A were derived. In particular, the energy U_0 for the onset of rotational damping is found to depend on the level density and on the strength of the two-body residual interaction, leading to the dependence $U_0 \propto A^{-2/3}$. In addition, the rotational damping width $\Gamma_{\rm rot}$, which is proportional to the statistical dispersion of the rotational frequencies of the cranked shell model np-nh states, is expected to follow the relation $\Gamma_{\rm rot} \propto I A^{-5/2} \epsilon^{-1}$, where I and ϵ are the spin and deformation, respectively.

To determine the validity of the relations given above, nuclei with similar deformations but with different masses have been compared, like ^{164}Yb ($A \approx 160$) and ^{114}Te ($A \approx 110$) [24], for which discrete rotational structures have been observed up to high spin values [31, 60].

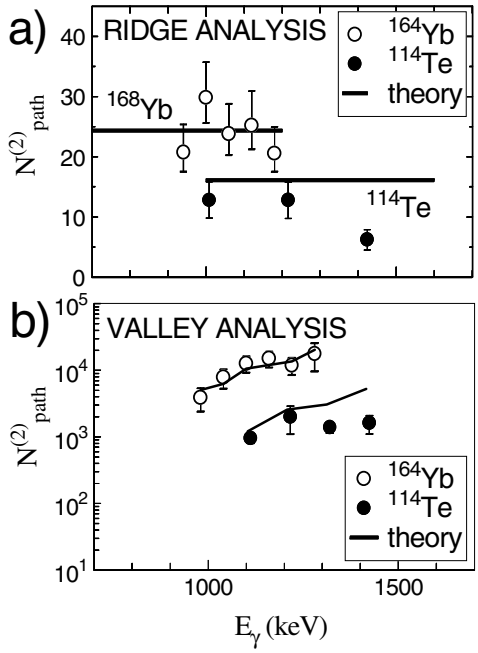

Figure 32. The number of decay paths $N_{\text{path}}^{(2)}$ extracted from the fluctuation analysis of the measured first ridge (panel (*a*)) and valley (panel (*b*)) of ^{164}Yb (open circles) and ^{114}Te (full circles) nuclei, in comparison with predictions from band mixing calculations (full lines) [10]. In the case of ^{164}Yb the data are compared with calculations for the rare earth nucleus ^{168}Yb [24].

As discussed in [24], the analysis has been performed on quasi-continuum spectra, which are found to display similar gross features both in single and double coincidence spectra.

Figure 32(*a*) shows the results obtained from the analysis of the ridge structures observed in γ–γ coincidence spectra of ^{114}Te, in comparison with the ^{164}Yb data previously discussed in section 7. In the case of ^{114}Te, because of the complex level scheme with high energy transitions at low spin the number of clean cuts for which the fluctuation analysis could be applied is more limited than for the ^{164}Yb nucleus. It is found that the number of paths deduced from the ^{114}Te data is on average approximately a factor of two smaller than in the ^{164}Yb case, as also observed for the ^{112}Sn nucleus of the same mass region [26].

The theoretical value for the number of discrete excited bands populating the ridge structures in γ–γ coincidence matrices was obtained from band mixing calculations by counting the number of two consecutive transitions having branching number $n_{\text{branch}} \leqslant 2$, as discussed in sections 3 and 6. The results, averaged over the spin interval 25–35$\hbar$, are shown by full lines for ^{114}Te and ^{168}Yb, the latter one describing the average features of the quasi-continuum of rare earth nuclei.

The number of paths $N_{\text{path}}^{(2)}$ obtained from the analysis of the valley region, collecting mostly damped transitions from states at which one expects the fragmentation of the rotational decay, is shown in figure 32(*b*). Also in this case a significant difference is seen between the results of ^{114}Te and ^{164}Yb data, in agreement with similar findings for ^{112}Sn [26]. The expected values of $N_{\text{path}}^{(2)}$ based on the same band mixed calculations used for the ridge analysis are shown by the full curves in figure 32(*b*). These predicted values were obtained by applying the fluctuation analysis technique to numerically calculated spectra produced by the simulation code MONTESTELLA, based on the calculated levels and transition probabilities for the specific nuclei, as discussed in section 3.2 [15]. As one sees from this figure, the calculations are found to reproduce both the ridge and the valley results quite well, giving strong support to the band mixing model [10] in different regions of masses.

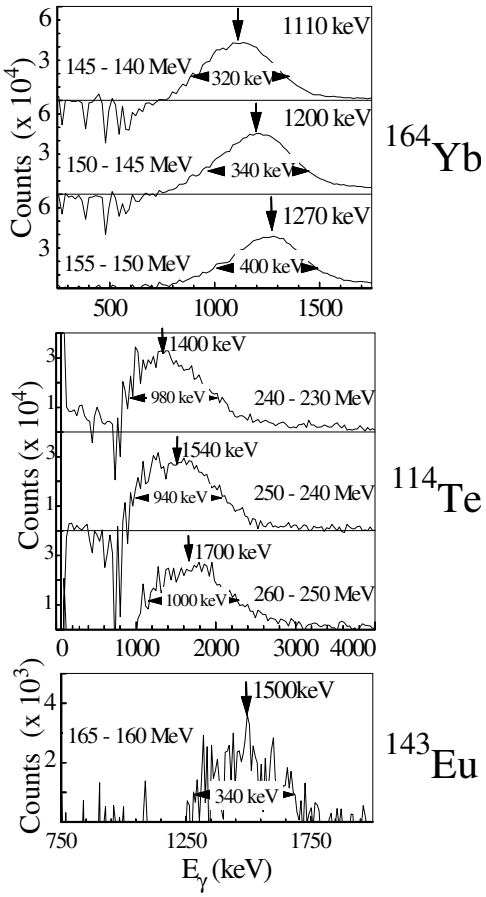

Figure 33. The continuous E2 bump obtained as a difference between 1D spectra at consecutive bombarding energies, for ^{164}Yb (top), ^{114}Te (middle) and ^{143}Eu (bottom). The difference in bombarding energies is given for each panel, together with the centroid and FWHM of the E2 distributions (adapted from [24, 26]).

Altogether, the present experimental results show that γ cascades of thermally excited deformed nuclei are governed by damped rotational motion, not just for rare earth nuclei, but also for the lighter $A = 110$ systems. In addition, the quantitative agreement between calculations and experiment seen in figure 32 strongly supports the scaling with mass number of the residual interaction and level density. According to the present calculation, damping should set in around heat energy $U_0 \approx 0.9$–1.0 MeV in ^{114}Te, compared with $U_0 \approx 0.7$–0.8 MeV in ^{168}Yb, which agrees rather well with the scaling $U_0 \propto A^{-2/3}$, originally proposed in [8]. In addition, the values of the damping widths predicted by the band mixing calculations are approximately a factor of two larger for ^{114}Te than for ^{168}Yb, as shown in figure 8, also in agreement with the scaling $\Gamma_{\rm rot} \propto IA^{-5/2}\epsilon^{-1}$ of the schematic model. Experimentally, this cannot be directly deduced from the number of paths in the valley, since $N^{(2)}_{\rm path}$ depends quadratically on $\Gamma_{\rm rot}$ but more strongly on the level density, although the satisfactory agreement between data and theory supports a proper modelling of the damping mechanism.

A value for $\Gamma_{\rm rot}$ can be inferred from the measured width of the E2 continuous distributions constructed as a difference between 1D spectra at consecutive bombarding energies, as shown in figure 33 for the ND nuclei ^{164}Yb (the same as in figure 2(b)) and ^{114}Te and for the SD nucleus

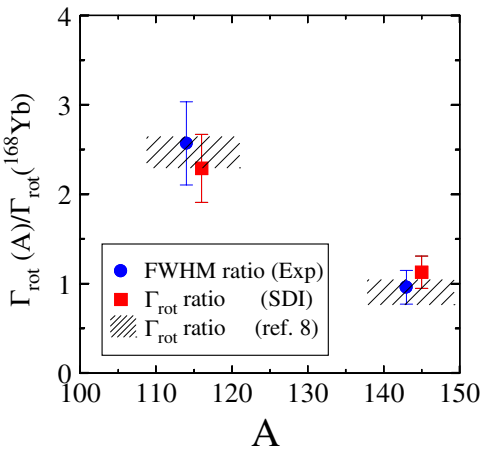

Figure 34. The scaling of the damping width Γ_{rot} with the mass number A, the deformation parameter ϵ and the spin I is tested for the ND nucleus ^{114}Te and for the SD nucleus ^{143}Eu, with respect to the ND nucleus ^{164}Yb. The shaded areas correspond to the ratio of the damping widths as expected according to the simple estimate $\Gamma_{rot} \propto I A^{-5/2} \epsilon^{-1}$ of [8], while the squares give the same ratio microscopically calculated by the band mixing model. The experimental values obtained from the width of the difference spectra of figure 33 are shown by circles.

^{143}Eu (later discussed in section 10) [24, 26, 61]. However, since all the decays from the entry distribution contribute to the difference spectrum, and not only E2 transitions corresponding to a given $I \rightarrow I - 2$ decay, the widths of the difference spectra can only be taken as an upper limit for the rotational damping width. In figure 33 the centroids and widths of the E2 distributions are indicated by arrows in each panel. Averaging over the given values one obtains FWHM $= 350 \pm 50$, 900 ± 100 and 340 ± 45 keV for ^{164}Yb, ^{114}Te and ^{143}Eu, respectively. These values can be used to test the scaling of Γ_{rot} with mass number and deformation, as shown in figure 34. In this figure, the ratios of the damping widths calculated according to the simple estimate of [8] are shown by a shaded area for ^{114}Te ($\epsilon = 0.25$) and ^{143}Eu ($\epsilon = 0.6$) with respect to ^{168}Yb ($\epsilon = 0.25$), assuming the spin values $I = 35 \pm 5$, 35 ± 5 and $54 \pm 5\hbar$ which correspond to the experimental conditions of the data reported in figure 33. The circles and squares given in the figure represent the ratios of the FWHM, as extracted from the E2 distributions of figure 33, and of the rotational damping widths calculated by the band mixing model and shown in figure 8. As one can see, consistency is found among all evaluations, supporting the dependence of Γ_{rot} on mass, deformation and spin as originally predicted [8].

One can then conclude that the dependence of the damping mechanism on the mass and deformation can be closely tested by studying the shapes and fluctuations carried by γ-coincidence spectra produced by excited rotating nuclei. In the cases studied the experimental results are well described by the existing model, although the rotational damping width Γ_{rot} appears to be a quantity still not easily accessible in experiments, as also discussed in section 11.

10. Superdeformation at finite temperature

Among the most striking results in the field of high-spin physics, there is the discovery of SD nuclei, namely of highly elongated prolate shapes with an axis ratio of approximately (2:1). Such weakly populated structures have been found in several regions of masses, such as $A = 150, 190, 130$ and 80 [62]. This has motivated further theoretical and experimental investigations, mainly aiming at understanding the mechanisms which allow us to observe these peculiar configurations over a wide spin interval, from the fission limit down to the angular momentum region where the SD yrast rather suddenly decays into the ND states. It is known now that this is possible due to the presence of different nuclear shapes, which can coexist over a wide spin range, being well separated by a potential energy barrier in the deformation space. This also explains the sudden decay-out of the SD rotational bands as a tunnelling process

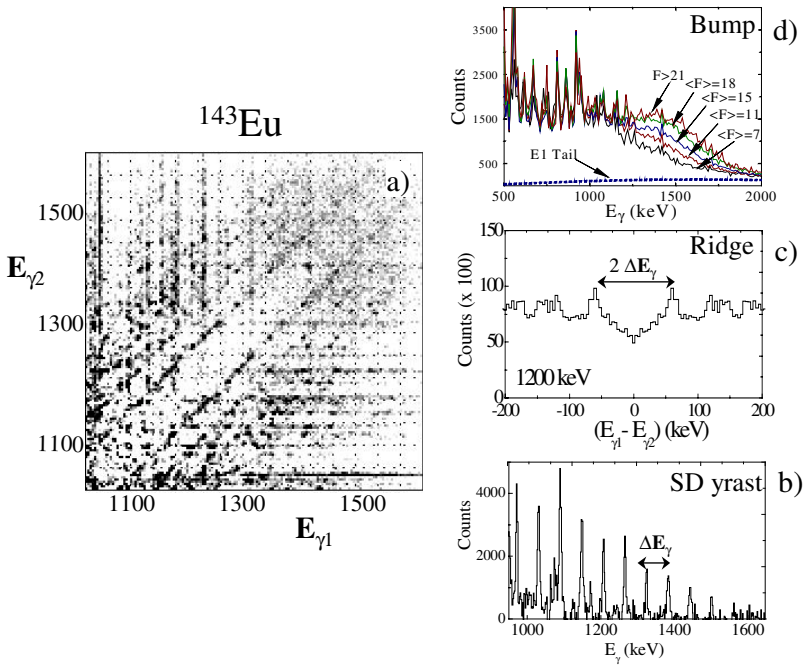

Figure 35. This figure shows the various SD rotational structures which can be observed in the nucleus ^{143}Eu starting from a γ–γ matrix (panel (*a*)): (*b*) the SD yrast, with a spacing $\Delta E_\gamma = 4\hbar^2/\Im^{(2)}$ between consecutive transitions; (*c*) the ridge structure, clearly visible in the 2D matrix (*a*) and in the perpendicular cuts (*c*), with a distance between the two innermost ridges equal to $2\Delta E_\gamma$; (*d*) the collective E2 bump observed in 1D spectra, which shows a moving edge as a function of the Ge fold (adapted from [27, 74]).

through the barrier between the SD and ND minima, caused by a statistical mixing between the SD states and the neighbouring ND states [63, 64]. This leads to highly fragmented decay sequences of a few γ-rays, linking the SD and ND potentials, which can be observed as discrete transitions only in rare cases [65, 66], while most of the decay-out intensity is found to produce a broad continuous distribution of statistical nature [67–70].

While this scenario has been extensively investigated in the case of the SD yrast and of the first few SD excited bands experimentally observed, fewer information is available on the thermally excited rotational motion in the SD well [27, 68, 71–73]. This is because it requires not only the experimental analysis of quasi-continuum spectra connected with the SD structures, but also the comparison with calculations describing both the thermally excited rotational motion and the barrier penetration effect. Nevertheless, the study of excited SD bands provides a unique opportunity to learn about the shape dynamics under the influence of the thermal and collective rotational degrees of freedom.

In this respect, one of the most extensively studied nuclei is ^{143}Eu, which shows a particularly strong population of the SD states at high angular momenta [27, 61, 68, 71]. This is a consequence of the low crossing between the normal and SD yrast lines, which occurs at relatively low angular momentum ($\approx 40\hbar$), as compared to the more typical case of ^{152}Dy. In fact, besides the SD yrast band with $\approx$2% intensity (see figure 35(*b*)), a pronounced ridge–valley structure, typical of rotational motion and with a moment of inertia corresponding to a SD nucleus with deformation $\epsilon \approx 0.55$, was observed in the high transition energy region of γ–γ coincidence spectra, as shown in figures 35(*a*) and (*c*). In addition, a strong E2 bump of SD

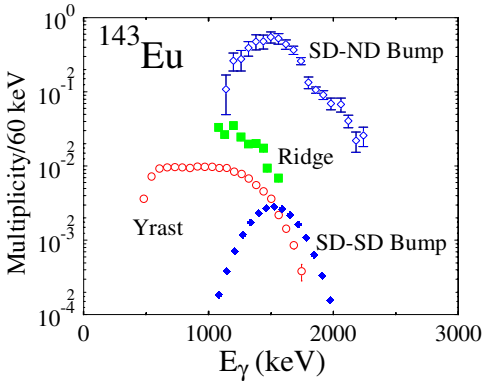

Figure 36. The intensity, per 60 keV interval, of the SD yrast transitions (circles), of the SD ridge (squares), of the SD quasi-continuum bump in coincidence with ND transitions (full diamonds) and with SD yrast transitions (open diamonds) in the nucleus ^{143}Eu (adapted from [27, 68]).

nature is found to develop in 1D spectra as a function of fold, as shown in figure 35(*d*) [27, 68]. In contrast, a very complex and irregular level scheme is observed in the low spin region, due to the existence of both spherical and triaxially deformed shapes [75]. Figure 36 shows the intensity of the SD structures experimentally observed in ^{143}Eu.

The collectivity of the various SD structures of ^{143}Eu has been measured using DSAM techniques, as reported in [71]. In the experiment, a ^{37}Cl beam at energies of 165 and 170 MeV impinged on a ^{110}Pd target 950 μg/cm^2 thick, with an Au backing of 15 mg/cm^2. In particular, in the case of the ridges, populated by discrete rotational bands of low excitation energy up to the region where rotational damping sets in (see section 2.2), the quadrupole moment of the excited rotational bands has been extracted by a DSAM technique which allowed us to make use of the entire statistics of the experiment. As described in [71], an energy-dependent Doppler correction, corresponding to a given quadrupole deformation Q_t, has been applied to the backed target data, on an event by event basis, in order to produce a number of γ–γ matrices, each corresponding to a different Q_t value (ranging from 3 to 13 eb in steps of 1 unit). After a COR background subtraction [4], with a reduction factor chosen in this case to be 0.95 to emphasize the high spin region, cuts perpendicular to the $E_{\gamma_1} = E_{\gamma_2}$ diagonal have been produced from the matrices over the transition energy region $\langle E_\gamma \rangle = 1120$ and 1300 keV, covered by the ridges. It is found that the ridge structure appears more and more clearly when a Doppler correction close to that of the SD yrast band of ^{143}Eu is applied, acquiring a minimum FWHM (consistent with a previous thin target experiment) for Q_t values of the order of 10 eb.

Figure 37 shows the fractional Doppler shift $F(\tau)$ experimentally obtained from the analysis of the SD yrast (circles) [76], ridges (squares) [71], E2 bump (open diamonds) [27] and triaxial transitions (full triangles) of ^{143}Eu [77], in comparison with the calculations from [76], corresponding to different values of the quadrupole moment Q_t. As one can see, the experimental results for the ridges and E2 bump are consistent with a large quadrupole deformation definitely closer to the SD yrast than to the triaxial structures, which represent the second largest known deformation in the nucleus ^{143}Eu, besides the SD one. This strongly supports the SD nature of the excited rotational bands, suggesting that the SD nucleus ^{143}Eu maintains its collectivity with increasing excitation energy, at least until damping sets in, as also observed in ND nuclei [21, 23]. In fact, the DSAM analysis of the E2 bump, performed according to [23, 27] (see also section 5), not only shows large error bars, but is also restricted to an energy region not so sensitive to the quadrupole deformation, giving only an upper limit ($\tau \leqslant 10^{-14}$ s) to the lifetimes of the E2 continuum. Therefore, a more conclusive study of the collectivity of the damped rotational motion would require us to focus on a lower transition energy region, where the fractional Doppler shift is expected to strongly deviate from 1. In

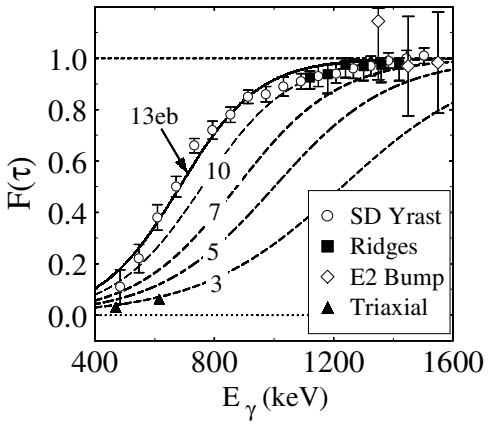

Figure 37. The measured fractional Doppler shifts for the SD yrast (circles), the SD ridges (squares), the E2 collective bump (diamonds) and the triaxial transitions (triangles) experimentally observed in the nucleus ^{143}Eu. The curves represent the expected theoretical values for the quadrupole moments $Q_t = 3, 5, 7, 10$ and 13 eb (adapted from [27, 71]).

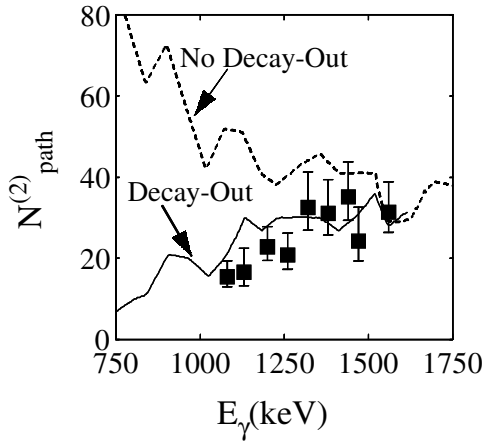

Figure 38. The number of excited rotational bands extracted by the fluctuation analysis of the SD ridges of ^{143}Eu (squares), compared with cranked shell model calculations including a two-body surface delta interaction (broken curve) [80]. The full curve represents the theoretical predictions including the decay-out process into the ND well [81] (adapted from [71]).

the case of ND nuclei, this has been done by studying the valley region of γ–γ coincidence matrices, applying the covariance technique discussed in sections 4 and 5. So far, in the case of SD nuclei the limited statistics collected along the valley region and the presence of intense transitions of lower deformation have turned out to be prohibitive for such an analysis, leaving the problem to be addressed by more selective and powerful future experiments.

The SD ridge structure observed in the high energy region of the γ–γ coincidence matrix of ^{143}Eu, sorted by applying the Doppler correction corresponding to the quadrupole moment of the ridges ($Q_t \approx 10$ eb), have been further investigated by the statistical analysis of the count fluctuations, as described in section 4. This has allowed us to estimate the total number of discrete excited SD rotational bands, which cannot be individually resolved due to their extremely weak population. In fact, the only known discrete excited SD band of ^{143}Eu is found to collect a maximum intensity of 35% of the SD yrast [78], which is at the observation limit of the present detection arrays.

The results of the fluctuation analysis of the ridge structures of ^{143}Eu are shown in figure 38 by squares. Before the statistical method is applied, all known discrete lines of the SD yrast band have been removed from the γ–γ spectrum by the Radware software program [46] in order to obtain the best estimate of the unresolved paths [14]. It is found that the number of SD excited discrete bands depends very strongly on the transition energy, reaching a constant value of $\approx$30 in the transition energy region 1300 keV $< E_\gamma <$ 1600 keV, where the SD ridge structure

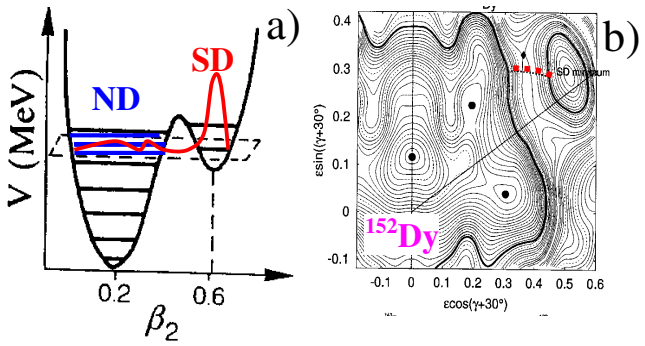

Figure 39. (*a*) The potential energy barrier separating the SD and the ND minima in the deformation space is shown, together with the vibrational states of the two wells. The wavefunction of a given SD state is shown to acquire a tail into the ND well, allowing the coupling of the SD state with the compound states in the first well. (*b*) The calculated potential energy surface for ^{152}Dy. The energy contour shown as a thick full curve and the least action path (broken curve) at this energy are also given (adapted from [63, 82]).

is populated, as shown in the intensity pattern of figure 36. In contrast, at lower transition energies the number of SD bands is found to decrease continuously, while the intensity of the ridge structure seems to increase and the intensity of the yrast band saturates. As shown in the figure, the experimental results have been compared with microscopic cranked shell model calculations plus a two-body SDI residual interaction for the specific nucleus ^{143}Eu [79, 80]. In fact, by counting the number of two consecutive transitions having a branching number n_{branch} less than or equal to 2 [10], as discussed in section 3.1, one can obtain the number of discrete excited rotational bands predicted by the model, together with the onset energy U_0 for rotational damping (corresponding to $n_{\text{branch}} = 2$), which in the case of ^{143}Eu is found to be ≈1.3–1.6 MeV above yrast. As shown in figure 38, the calculation (broken curve) is close to the data at the maximum of the distribution, while it deviates strongly at lower transition energies. This is generally expected for the lower part of the ridge structure, as a consequence of the barrier penetration into the first well.

The reduction in the measured number of excited SD bands can be reproduced by the model, when the decay-out mechanism of the excited states is taken into account (full curve) [81, 82]. In the model, the SD states obtained by cranking calculations are coupled to normally deformed compound states which lie energetically near, as schematically illustrated in figure 39(*a*). The coupling, as discussed in [63, 83] in connection with the decay-out of the SD yrast, is described in terms of a quantum tunnelling through the potential energy barrier in the deformation space, leading some components of the ND states to be mixed into the SD state. Since the ND states also have an associated electromagnetic transition probability, the SD state thus mixed will have the possibility of decaying not only with rotational E2 transitions within the SD well, but also with γ-rays feeding to the normal states, thereby giving rise to the decay-out into the ND well. An average decay-out probability can then be calculated for any specified value of spin and excitation energy of the SD rotational states, according to the expression:

$$\langle N_{\text{out}} \rangle \approx \sqrt{\frac{\Gamma_t}{D_{\text{ND}}} \frac{\Gamma_{\text{ND}}}{\Gamma_{\text{SD}}}}. \tag{12}$$

In the previous relation $\Gamma_{\text{ND}}/\Gamma_{\text{SD}}$ is the ratio between the electromagnetic decay widths in the ND and SD well, D_{ND} is the average spacing between states in the ND well and Γ_t is the

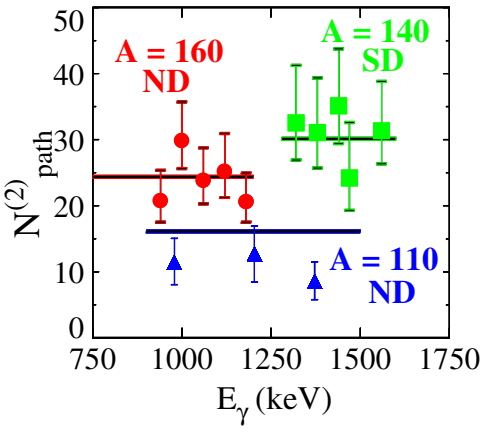

Figure 40. The number of decay paths $N^{(2)}_{\rm path}$ extracted by the fluctuation analysis of the first ridge of γ–γ matrices collecting the decay flow of nuclei with different masses and deformations. The circles give the experimental values for a typical ND nucleus of the $A = 160$ region (^{164}Yb), the triangles give the average values obtained for the ^{114}Te and ^{112}Sn lighter ND nuclei of mass $A \approx 110$, while the squares correspond to the experimental values measured for the SD nucleus ^{143}Eu at the highest transition energies. The predictions from band mixing calculations for the specific nuclei are represented by full lines.

tunnelling decay width of the excited SD rotational state. This latter quantity can be evaluated semiclassically as a product of three terms:

$$\Gamma_t = \frac{\hbar\omega_{\rm SD}}{2\pi}\frac{D_{\rm SD}}{\hbar\omega_{\rm SD}}(1+\exp 2S)^{-1}. \tag{13}$$

Here $\hbar\omega_{\rm SD}/2\pi$ is the knocking frequency at the barrier (with $\omega_{\rm SD}$ being the vibrational frequency of the collective motion in the SD minimum), $T = (1+\exp 2S)^{-1}$ is the tunnelling transmission coefficient (with S being the classical action integral of a given tunnelling path in the $\beta-\gamma$ deformation plane, as shown in figure 39(b) in the case of ^{152}Dy), and $D_{\rm SD}/\hbar\omega_{\rm SD}$ is a reduction factor (which becomes 1 for the SD yrast), due to the distribution of the collective vibrational excited SD states over many compound states. From equation (13) one finds that the largest tunnelling decay width corresponds to the tunnelling path with the least action integral.

One can then conclude that the satisfactory agreement between the data and the number of SD bands predicted by the microscopic calculations, also including the decay-out mechanism, not only provides a clear evidence for a tunnelling process in the thermally excited nucleus, but also gives further support to the validity of the band mixing model, which is found to properly describe the thermally excited rotational motion in different regions of mass and deformation [10,16,79,80]. This is illustrated even more clearly in figure 40, where the number of SD bands of ^{143}Eu, measured in the region 1300 keV $< E_\gamma <$ 1600 keV not affected by the decay-out process, is compared with the band mixing model predictions, together with similar results for ND nuclei of mass $A \approx 110$ and 160.

The study of the quasi-continuum in the SD nucleus ^{143}Eu has also been an essential tool for the understanding of the feeding mechanism of the SD states. In fact, since the discovery of the first SD yrast band [84, 85], one of the most outstanding problems was the population of such structure which, at the highest spins, is found to be one order of magnitude larger than in normally deformed nuclei, as clearly shown in figure 41. To explain this finding it has been proposed that the cooling of the residual nucleus by statistical E1 could be an important mechanism leading to the population of the SD states [86, 87]. This is because the E1 transition probability at $E_\gamma \approx$ 8–10 MeV for the decay of the giant dipole resonance (GDR) built on SD configurations is expected to be larger than for ND states, both due to the shape of the strength function and to the level density of SD states [88]. Although several attempts have been made in the last decay to find experimental evidence for the E1 feeding of SD states, no conclusive answer could be given to the problem, mainly due to the experimental limitations of the set-ups used [89–91]. In the ^{143}Eu experiment previously discussed, the

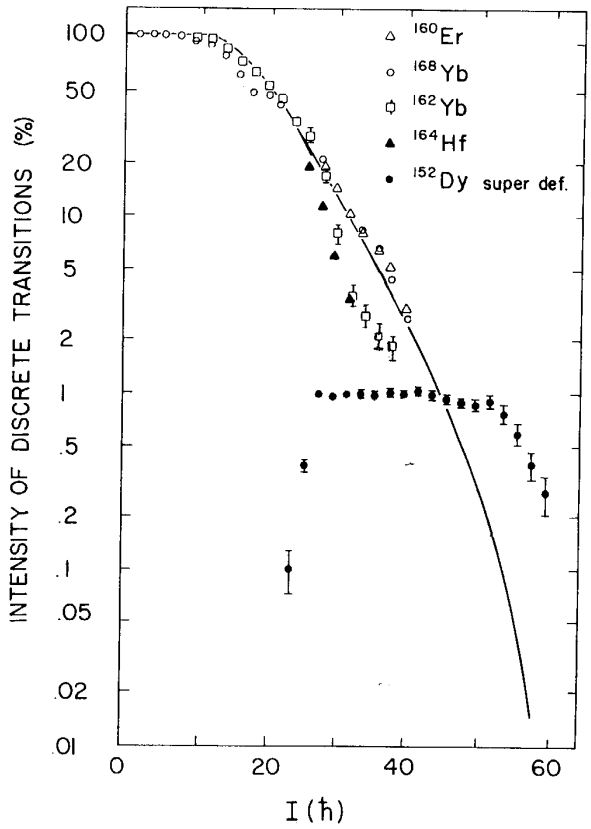

Figure 41. Discrete line intensities normalized to the $2^+ \rightarrow 0^+$ ground state transition, for the well deformed nuclei ^{160}Er, ^{180}Yb and ^{164}Hf and for the SD band of ^{152}Dy. The intensities plotted are the sum of all observed discrete lines at the given spin. The full curve shows the calculated discrete line intensity for the case of ^{168}Yb (adapted from [86]).

EUROBALL array, employed to detect low-energy discrete lines, was combined with 8 large-volume BaF_2 scintillators detectors for the high-energy γ-rays [92, 93]. The effect of the E1 population of the SD states by the γ decay of the GDR built on a SD nucleus has been investigated by measuring the relative intensity of the SD band, the ridge structure and the E2 bump at different values of the gating high-energy γ-rays. As shown in figure 42, the relative intensities of the SD yrast (squares), SD ridges (triangles) and E2 bump (circles) are found to rapidly increase with the high-energy gating transition, following the ratio between the SD GDR strength function and the spherical one (full curve). One can then conclude that the enhanced feeding of the SD structures consistently shows the important role played by the E1 emission from the GDR built on SD states in the population of such highly deformed shapes.

11. Futures perspectives: damping width and compound width

In spite of the extensive work carried out in the field of rotational motion at finite temperature, reviewed in this paper, several open problems still remain to be addressed. Among them, there is the direct measurement of the spreading width of the B(E2) strength, namely the rotational damping width $\Gamma_{\rm rot}$. As discussed in section 9, such a quantity appears not to be

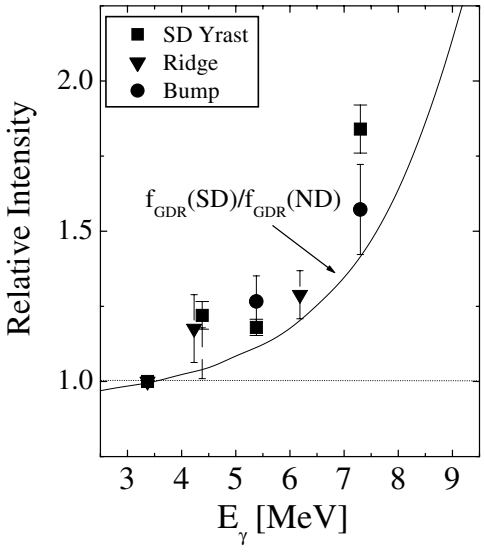

Figure 42. Intensity of the SD yrast band (squares), ridges (triangles) and E2 bump (circles) of ^{143}Eu, as a function of the high-energy gating transition, normalized at 3 MeV. The full curve represents the ratio between the SD and the spherical GDR strength functions, giving a lower limit for the feeding of the SD nucleus by E1-decay from the GDR [92].

easily accessible, since it is difficult to isolate experimentally excited rotational transitions corresponding to a given $I \rightarrow I - 2$ decay.

Several attempts have been made in this direction, mostly based on comparison between experimental and numerically calculated γ-ray coincidence spectra [11, 15, 94]. However, due to the strong dependence on the simulation parameters and on the initial conditions of the γ cascades, as also discussed in sections 3.2 and 9, no definite estimates of the damping width could be obtained, but only largely uncertain values, ranging from 100–350 keV for ^{168}Yb, a typical ND nucleus of the rare earth region.

As an alternative technique, the *rotational plane mapping* method (RPM), mostly based on the analysis of double and triple coincidence spectra, aimed at the separation of the contributions from damped and undamped transitions and at a direct extraction of $\Gamma_{\rm rot}$ from the analysis of the shape of the spectra [95, 96]. In such a context it was assumed that the rotational transition in each step of the cascade may select its energy from the full B(E2) strength distribution of width $\Gamma_{\rm rot}$, independently of the preceding transitions, meaning that the γ transitions of the damped rotational cascades are *uncorrelated*. This would lead to 2D coincidence spectra characterized by a valley along the $E_{\gamma_1} = E_{\gamma_2}$ diagonal, its width and depth being related to the rotational damping width, as illustrated by the simple simulation calculations shown in figure 43. As one can see, according to the assumption of independent selection of γ transitions, the average transition energies will form a grid of hills, with a full width at half maximum equal to $\Gamma_{\rm rot}$ in all directions, and with a spacing $\Delta E_\gamma = 4\hbar^2/\Im^{(2)}$ determined by the effective moment of inertia. In particular, no hills are expected along the central diagonal, since in a regular rotational cascade no γ-ray transitions with the same energies can be present. It is found, as shown in figures 43(c) and (g), that for values of $\Gamma_{\rm rot}$ comparable to or larger than $4\hbar^2/\Im^{(2)}$ the hills merge together and only the central valley can still be recognized. This implies that the shape of the B(E2) strength will determine the shape of the central valley, whose width and depth can be directly related to the rotational damping width $\Gamma_{\rm rot}$. As discussed in [96], analytical expressions can be worked out, describing the distributions of damped events in 2D as well as in 3D coincidence spectra, assuming a given form for the B(E2) strength function. This is illustrated in figure 43(d) in the case of double coincidence spectra.

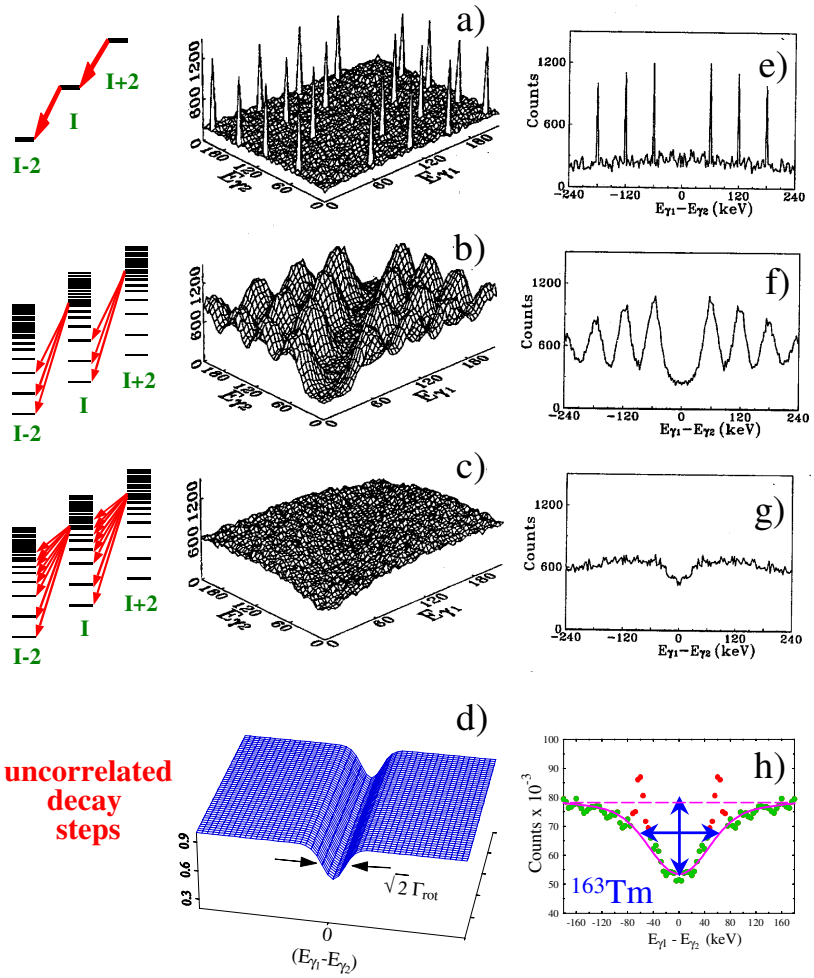

Figure 43. Schematic illustration of the generation of a γ–γ coincidence spectrum, under the simple assumption of *uncorrelated* decay steps [96]. Panels (*a*), (*b*) and (*c*) show double coincidence spectra produced by schematic simulation calculations, using the damping width $\Gamma_{\rm rot} = 0, 30, 60$ keV. The corresponding perpendicular cuts across the $E_{\gamma 1} = E_{\gamma 2}$ diagonal are given in panels (*e*), (*f*) and (*g*), respectively. In the bottom of the figure, panel (*d*) shows the analytical function representing the intensity distribution of damped transitions (with $\Gamma_{\rm rot} = 100$ keV) in the 2D coincidence spectrum, whose width and depth can be related to the rotational damping width. Panel (*h*) shows, as an example, a perpendicular cut on a γ–γ spectrum of ^{163}Tm (dots), while the full curve gives a fit of the damped component according to the analytical function shown in (*d*) (adapted from [96]).

The RPM, used to fit the valley shape of 2D and 3D coincidence spectra of ^{168}Yb and ^{163}Tm nuclei [95,96] (see figure 43(*h*)), provided a first direct estimate of the rotational damping width of the order of $\approx$100 keV at $I \approx 40\hbar$, which is almost a factor of 2 lower than expected from the model [8,10]. However, this result has to be taken with some caution, since the measured ratio between the width and depth of the valley was in disagreement with the simple assumption of uncorrelated rotational decay at the basis of the method. This suggested that the strength function associated with the decay of two consecutive quadrupole rotational transitions, and so far related only to the spreading width $\Gamma_{\rm rot}$, could display a more complex structure, made of a wide and a narrow component. In particular, the latter could be more directly related

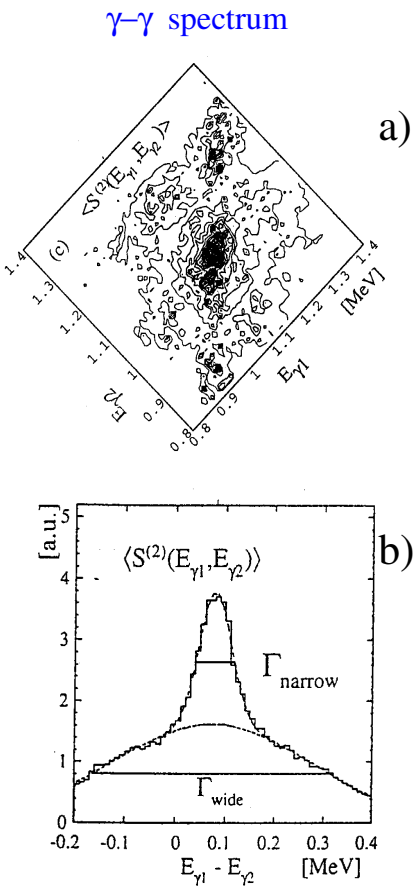

Figure 44. Panel (*a*) shows the average two-step strength function $\langle S^{(2)}(E_{\gamma_1}, E_{\gamma_2})\rangle$ for the 51st–100th lowest levels of each configurations at spin $I = 42, 43\hbar$, as obtained from the band mixing calculations including a surface delta interaction described in [10]. Panel (*b*) shows the corresponding projection on the E_{γ_1}–E_{γ_2} axis. The width of the narrow and wide component are also indicated (adapted from [97]).

to rotational correlations carried over consecutive decay steps, surviving as scars of discrete rotational motion high up in the region of rotational damping [35].

The assumptions underlying the damping model have been more closely investigated, making use of the microscopic band mixing calculations discussed in section 3.1 [10, 97]. As shown in figure 44, the calculated γ–γ coincidence spectra from the excitation energy region $U = 1$–2 MeV, which is where the major part of the γ flow goes (see section 3.2 and figure 11), show a profile which can be decomposed into two distinct distributions, having a wide and a narrow width. Such complex line shape can be related to the fine structure of the B(E2) strength which is expected to carry information not only on the spreading of the rotational frequencies, namely the rotational damping width $\Gamma_{\rm rot}$, but also on a much more fundamental quantity such as the spreading width of the *n*p-*n*h configurations, namely the compound nucleus width Γ_μ. This is a consequence of the mixing between the unperturbed cranked shell model states, which distribute over the compound nucleus states with a spreading width Γ_μ, as schematically illustrated in figure 45.

In particular, the calculations show a direct relation between the spreading widths Γ_μ and $\Gamma_{\rm rot}$ and the width of the narrow and wide components observed in γ–γ coincidence spectra [97] (see figure 44), namely:

$$\Gamma_{\rm narrow} = 2\Gamma_\mu \tag{14}$$

$$\Gamma_{\rm wide} = 2\Gamma_{\rm rot}. \tag{15}$$

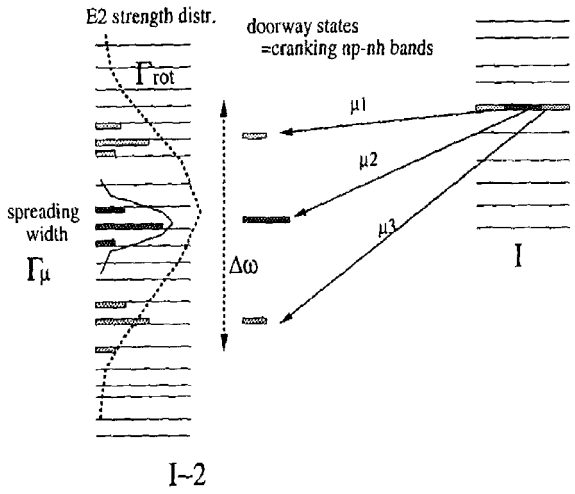

Figure 45. Schematic illustration of damped E2 transitions in rotating nuclei. The horizontal bars represent the energy levels at spin I and $I - 2$. The thick bars represent the strength of cranked shell model np-nh states (from [16]).

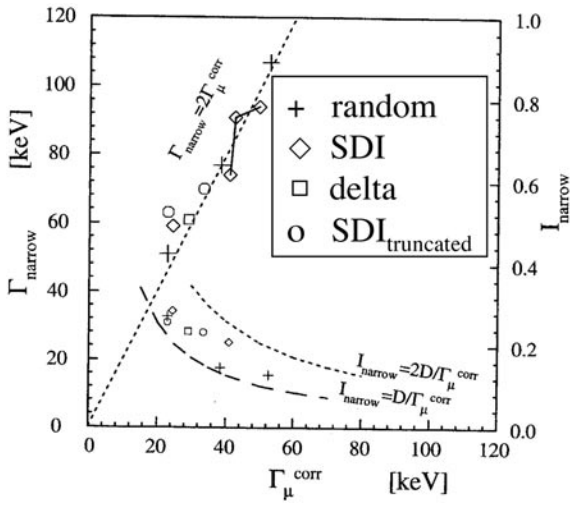

Figure 46. The values of the width Γ_{narrow} (large symbols, left axis) and the intensity I_{narrow} (small symbols, right axis), associated with the narrow component extracted from the two-step strength function from band mixing calculations (see figure 44), are plotted versus the compound spreading width Γ_μ. Different residual interactions are used, as indicated in the legend, and the averages are taken over the level 51–100 for the spin interval $I = 30$–$51\hbar$ (adapted from [97]).

The linear relation between Γ_μ and Γ_{narrow}, expressed by equation (14), is shown in figure 46 for band mixing calculations of ^{168}Yb, assuming different types of residual interactions, as indicated in the legend. On the same figure, the dependence of the intensity of the narrow component on the compound width is also shown (right axis). This is found to be in satisfactory agreement with the theoretical expectation $I_{\text{narrow}} = D/\Gamma_\mu$, with D being the average level spacing [97].

The microscopic calculations have been carried out for several ND and SD nuclei in different mass regions, showing large variations in the rotational damping width, as already discussed

in section 3.1, while more or less similar values (of the order of ≈50 keV) are predicted for the compound nucleus width, which is always found to be smaller than $\Gamma_{\rm rot}$ [16]. A first attempt in the search of the narrow component in experimental 3D spectra can be found in [98].

One can then conclude that a revised analysis of the ridge–valley structures present in 2D and 3D quasi-continuum γ coincidence spectra can become instrumental in the study of the complex mechanism of the damping of rotational motion and on the interplay between rotational damping and compound nucleus damping. In particular, the possibility of directly extracting the compound width Γ_μ from the data seems to be even more challenging and would represent a major breakthrough in nuclear spectroscopy in general. In fact, although Γ_μ plays a central role in basic nuclear phenomena, such as the statistical and chaotic features of energy levels [99–101] and the damping of collective vibrations [102, 103], only scarce and indirect experimental information are presently available, mostly based on a highly controversial quantity, both theoretically and experimentally, such as the single-particle width [104–107].

In addition, other scenarios still remain to be explored for warm rotating nuclei, such as for example the regime of ergodic rotational bands, which has been predicted to occur in nuclei with large deformation when chaotic intrinsic states are combined with ordered rotational motion [17, 18]. Also the vanishing of the quantum numbers associated with the nuclear rotation, as the ultimate transition from the order to the chaotic compound regime, remains to be experimentally investigated in detail, requiring the highest selectivity from detector arrays of future generations.

12. Conclusions

In this review we have presented and discussed several properties of warm rotating nuclei, as deduced from their γ decay. In particular, we have shown that the use of the *fluctuation analysis method* has allowed us to make a major breakthrough on several important issues. Among them, the importance of the two-body residual interaction, the collectivity of the excited rotational states, the conservation of the quantum numbers, the dependence of the band mixing process on mass and deformation and the decay-out of the SD excited bands were addressed by applying these techniques to the experimental data and theory. The main relevant result is the experimental evidence for the damping of rotational motion. In addition, it is found that, indeed, well deformed nuclei maintain their collectivity with increasing temperature, the quantum numbers are partially conserved in the damping region, and the band mixing process follows simple scaling laws for the dependence on mass and deformation, as predicted by the model. However, there are still many interesting questions to be answered, the most pressing being a direct experimental determination of the rotational damping width, which requires very selective data together with further developments of the analysis techniques.

Acknowledgments

The review presented here is based on several works made in the last 10 years in the field of quasi-continuum spectroscopy. The authors wish to thank in particular Bent Herskind and T Døssing for introducing them with enthusiasm and illuminating discussions to this fascinating subject and for giving a major contribution to the development of the techniques and also to the work presented here. In addition, for the theoretical developments we thank R A Broglia, E Vigezzi and M Matsuo. Our experimental colleagues who have worked very closely with us, namely F Camera, G Benzoni, P Bosetti, S Frattini, A May, B Million and G B Hagemann, are gratefully acknowledged for the experimental support within the EUROBALL collaboration, which made possible the realization and the analysis of the experiments discussed here.

References

[1] Deleplanque M A *et al* 1978 *Phys. Rev. Lett.* **40** 629
[2] Deleplanque M A *et al* 1978 *Phys. Rev. Lett.* **41** 1105
[3] Love D J G *et al* 1985 *Phys. Rev. Lett.* **54** 1361
[4] Andersen O *et al* 1979 *Phys. Rev. Lett.* **43** 687
[5] Herskind B 1980 *J. Physique* C **10** 106
[6] Draper J E *et al* 1986 *Phys. Rev. Lett.* **56** 309
[7] Leander G 1982 *Phys. Rev.* C **25** 2780
[8] Lauritzen B, Døssing T and Broglia R A 1986 *Nucl. Phys.* A **457** 61
[9] Broglia R A *et al* 1987 *Phys. Rev. Lett.* **58** 326
[10] Matsuo M *et al* 1997 *Nucl. Phys.* A **617** 1
[11] Bacelar J C *et al* 1985 *Phys. Rev. Lett.* **55** 1858
[12] Stephens F S *et al* 1986 *Phys. Rev. Lett.* **57** 2912
[13] Herskind B *et al* 1992 *Phys. Rev. Lett.* **68** 3008
[14] Døssing T *et al* 1996 *Phys. Rep.* **268** 1–84
[15] Bracco A *et al* 1996 *Phys. Rev. Lett.* **76** 4484
[16] Matsuo M *et al* 1999 *Nucl. Phys.* A **649** 379c
[17] Bohr Aa and Mottelson B 1981 *Phys. Scr.* **24** 71
[18] Åberg S 1992 *Proc. Nucl. Part. Phys.* **28** 11
[19] Nordlund A *et al* 1995 *Nucl. Phys.* A **591** 117
[20] Nolan P J 1994 *Rev. Nucl. Part. Sci.* **45** 561
[21] Frattini S *et al* 1998 *Phys. Rev. Lett.* **81** 2659
[22] Leoni S *et al* 2000 *Nucl. Phys.* A **671** 71
[23] Million B *et al* 1997 *Phys. Lett.* B **415** 321
[24] Frattini S *et al* 1999 *Phys. Rev. Lett.* **83** 5234
[25] Garrett G, Hagemann G B and Herskind B 1986 *Ann. Rev. Nucl. Part. Sci.* **36** 419
[26] Bracco A *et al* 2000 *Nucl. Phys.* A **673** 64
[27] Leoni S *et al* 1996 *Phys. Rev. Lett.* **76** 3281
[28] Stephens F 1983 *Phys. Scr.* T **5** 5
[29] Deleplanque M A *et al* 1983 *Phys. Rev. Lett.* **50** 499
[30] Nolan P J *et al* 1990 *Nucl. Phys.* A **520** 657
[31] Fitzpatrick A *et al* 1995 *Nucl. Phys.* A **582** 335
[32] Leoni S, Bracco A, Døssing T, Herskind B, Lisle J C, Matsuo M, Vigezzi E and Wrzesinski J 1999 *Eur. J. Phys.* A **4** 229
[33] Åberg S 1990 *Phys. Rev. Lett.* **26** 3119
[34] Faessler A 1968 *Fortschr. Phys.* **16** 309
[35] Broglia R A *et al* 1996 *Z. Phys.* A **356** 259
[36] Matsuo M *et al* 1993 *Phys. Rev. Lett.* **70** 2694
[37] Matsuo M *et al* 1997 *Nucl. Phys.* A **A620** 296
[38] Døssing T and Vigezzi E 1995 *Nucl. Phys.* A **587** 13
[39] Aberg S 1988 *Nucl. Phys.* A **477** 18
[40] Schiller A, Bergholt L, Guttormsen M, Melby E, Rekstad J and Siem S 2000 *Nucl. Instrum. Methods* A **447** 498
[41] Melby E *et al* 1999 *Phys. Rev. Lett.* **83** 3150
[42] Guttormsen M *et al* 2000 *Phys. Rev.* C **62** 024306
[43] Leander G 1988 *Phys. Rev.* C **38** 728
[44] Stephens F S 1988 *Int. Conf. on Contemporary Topics in Nuclear Structure Physics* ed R Casten, A Frank, M Moshinsky and S Pittel (Singapore: World Scientific) p 297
[45] Hansen P G, Jonson B and Richter A 1990 *Nucl. Phys.* A **518** 13
[46] Radford D C 1995 *Nucl. Instrum. Methods* A **361** 297
[47] Frattini S *et al* 1999 *Nucl. Phys.* A **469** 387c
[48] Bacelar J C *et al* 1986 *Phys. Rev. Lett.* **57** 3019
[49] Northcliffe L C and Schilling R F 1970 *Nucl. Data Tables* **7** 233
[50] Ziegler J F and Chu W K 1974 *Nucl. Data Tables* **13** 463
[51] Hagemann G B *et al* 1997 *Nucl. Phys.* A **618** 199
[52] Bark R A *et al* 1995 *Nucl. Phys.* A **591** 265
[53] Bosetti P *et al* 1996 *Phys. Rev. Lett.* **76** 1204

[54] Bark R A *et al* 1997 *Z. Phys.* A **359** 5
[55] Døssing T *et al* 1999 *Nucl. Phys.* A **469** 370c
[56] Rekstad J, Tveter T S and Guttormsen M 1990 *Phys. Rev. Lett.* **65** 2122
[57] Soloviev V G 1993 *Phys. Lett.* B **317** 501
[58] Bohigas O, Giannoni M J and Schmit C 1984 *Phys. Rev. Lett.* **52** 1
[59] Mottelson B 1993 *Nucl. Phys.* A **557** 717c
[60] Thorslund I *et al* 1995 *Phys. Rev.* C **52** R2839
[61] Atac A *et al* 1993 *Phys. Rev. Lett.* **70** 1069
[62] Singh B, Firestone R B and Chu S Y F 1997 *Report* No LBL-38004
[63] Vigezzi E *et al* 1990 *Phys. Lett.* B **249** 163
[64] Khoo T L 1998 *Tunneling in Complex Systems Proc. from the Institute of Nuclear Theory* ed S Tomsovic (Singapore: World Scientific) p 229
[65] Khoo T L *et al* 1996 *Phys. Rev. Lett.* **76** 1583
[66] Ataç A *et al* 1996 *Z. Phys.* A **355** 343
[67] Henry R G *et al* 1994 *Phys. Rev. Lett.* **73** 777
[68] Leoni S *et al* 1997 *Phys. Lett.* B **409** 71
[69] Lopez-Martens A P *et al* 1996 *Phys. Rev. Lett.* **77** 1707
[70] Lopez-Martens A P *et al* 1999 *Nucl. Phys.* A **647** 217 and references therein
[71] Leoni S *et al* 2001 *Phys. Lett.* B **498** 137
[72] Farget F *et al* 1998 *Phys. Rev.* C **58** 150
[73] Twin P J 1990 *Nucl. Phys.* A **520** 17c
[74] Leoni S *et al* 1995 *Phys. Lett.* B **353** 179
[75] Piiparinen M *et al* 1996 *Nucl. Phys.* A **605** 191
[76] Forbes S A *et al* 1995 *Nucl. Phys.* A **584** 149
[77] Piiparinen M *et al* 1995 *Phys. Rev.* C **52** R1
[78] Axelsson A *et al* 1999 *Eur. Phys. J.* A **6** 175
[79] Yoshida K and Matsuo M 1997 *Nucl. Phys.* A **612** 26
[80] Yoshida K and Matsuo M 1998 *Nucl. Phys.* A **636** 169
[81] Shimizu Y *et al* 2001 *Nucl. Phys.* A **682** 464c
[82] Yoshida K, Matsuo M and Shimizu Y R *Nucl. Phys.* A in print
[83] Shimizu Y R, Vigezzi E, Døssing T and Broglia R A 1993 *Nucl. Phys.* A **557** 99c
[84] Twin P J *et al* 1986 *Phys. Rev. Lett.* **57** 811
[85] Hass B *et al* 1988 *Phys. Rev. Lett.* **60** 503
[86] Schiffer K, Herskind B and Gascon J 1989 *Z. Phys.* A **332** 17
[87] Herskind B *et al* 1987 *Phys. Rev. Lett.* **59** 2416
[88] Gallardo M, Diebel M, Døssing T and Broglia R A 1985 *Nucl. Phys.* A **443** 415
[89] Hass B *et al* 1990 *Phys. Lett.* B **245** 13
[90] Taras P *et al* 1988 *Phys. Rev. Lett.* **61** 1348
[91] Zhu L H *et al* 1997 *Phys. Rev.* C **55** 1169
[92] Bracco A, Camera F and Leoni S 2001 *Nucl. Phys.* A **682** 449c
[93] Bracco A *et al* 2000 *Phys. Scr.* T **88** 182
[94] Stephens F S, Draper J E, Bacelar J C, Beck E M, Deleplanque M A and Diamond R M 1987 *Phys. Rev. Lett.* **58** 2186
[95] Herskind B *et al* 1992 *Phys. Lett.* B **276** 4
[96] Leoni S *et al* 1995 *Nucl. Phys.* A **587** 513
[97] Matsuo M *et al* 1999 *Phys. Lett.* B **465** 1
[98] Døssing T *et al* 2001 *Nucl. Phys.* A **682** 439c
[99] Mottelson B R 1993 *Nucl. Phys.* A **557** 717c
[100] Zelevinsky V *et al* 1996 *Phys. Rep.* **276** 85
[101] Persson P and Åberg S 1995 *Phys. Rev.* E **52** 148
[102] Lauritzen B *et al* 1988 *Phys. Lett.* B **207** 238
[103] Lauritzen B *et al* 1995 *Phys. Rev. Lett.* **95** 5190
[104] Mahaux C and Sartor R 1991 *Adv. Nucl. Phys.* **20**
[105] Bertsch G *et al* 1979 *Phys. Lett.* B **80** 161
[106] Bertsch G *et al* 1983 *Rev. Mod. Phys.* **55** 287
[107] Donati P *et al* 1996 *Z. Phys.* A **354** 249